Final Report

# Shoreline Movement along the Texas Gulf Coast, 1930s to 2019

Jeffrey G. Paine and Tiffany Caudle

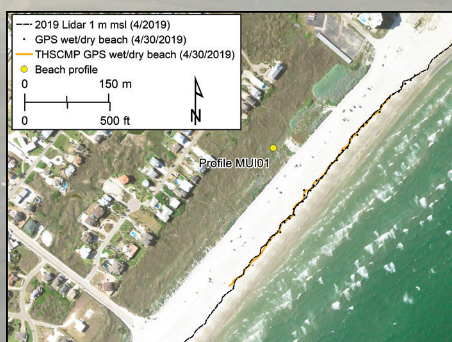


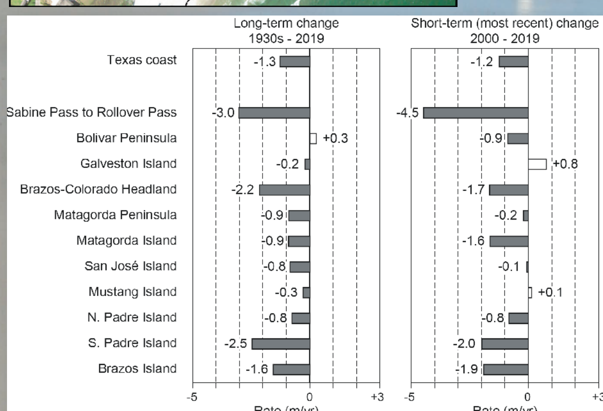


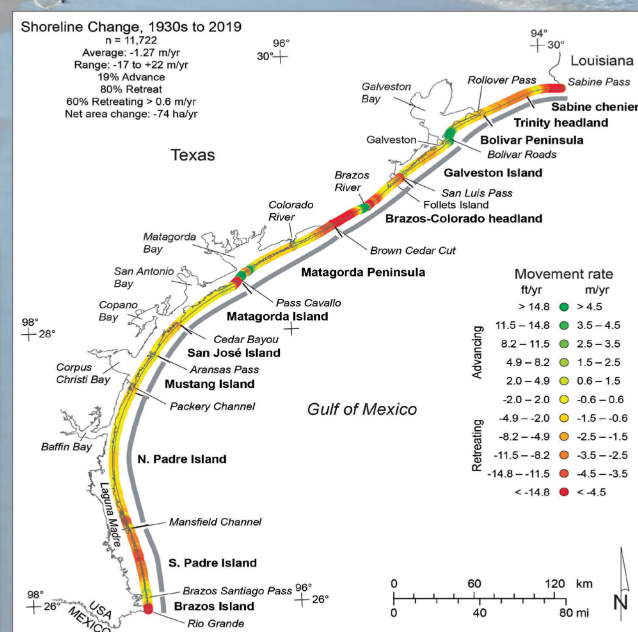


**Bureau of Economic Geology**
Scott W. Tinker, Director
Jackson School of Geosciences
The University of Texas at Austin
Austin, Texas 78713-8924

January 2020

Report prepared for
General Land Office under
contract no. 16-201-000,
CEPRA Project No. 1662,
Work Order No. B428.

QAe8472

*Page intentionally blank*

# SHORELINE MOVEMENT ALONG THE TEXAS GULF COAST,

# 1930s to 2019

by

Jeffrey G. Paine and Tiffany L. Caudle

Bureau of Economic Geology
John A. and Katherine G. Jackson School of Geosciences
The University of Texas at Austin
University Station, Box X
Austin, Texas 78713

*Corresponding author*
jeff.paine@beg.utexas.edu
(512) 471-1260
TBPG License No. 3776

Final Report Prepared for the General Land Office
under Contract No. 16-201-000, Work Order No. B428
CEPRA Project No. 1662

January 2020; Revised April 2020

*Page intentionally blank*

## CONTENTS



## FIGURES

TABLES

*Page intentionally blank*

ABSTRACT

Long-term rates of Gulf shoreline movement along the Texas coast have been determined through 2019 from a series of shoreline positions that includes those depicted on aerial photographs from the 1930s to 2007, ground GPS surveys from the 1990s, and airborne lidar surveys in 2000, 2012, and 2019. Net rates of long-term shoreline movement measured at 11,722 sites spaced at 50 m (164 ft) along the 590 km (367 mi) of Texas shoreline fronting the Gulf of Mexico average 1.27 m/yr (4.2 ft/yr) of retreat. Net shoreline retreat occurred along 80 percent of the Texas Gulf shoreline, resulting in an estimated net land loss of 6,627 ha (16,375 ac) since 1930 at an average rate of 74 ha/yr (184 ac/yr). Average rates of movement are more recessional on the upper Texas coast (net retreat at 1.71 m/yr [5.6 ft/yr] from Sabine Pass to the Colorado River) than they are on the middle and lower coast (net retreat at 0.97 m/yr [3.2 ft/yr] from the Colorado River to the Rio Grande).

Areas undergoing significant net retreat include: (1) the muddy marshes on the upper Texas coast between Sabine Pass and High Island; (2) segments on the sandy barrier-island shoreline on Galveston Island; (3) most of the combined fluvial and deltaic headland constructed by the Brazos and Colorado rivers; (4) sandy, headland-flanking barriers northeast (Follets Island) and southwest (Matagorda Peninsula) of the Brazos–Colorado headland; (5) San José Island, a sandy barrier island on the middle Texas coast; (6) the northern end and much of the southern half of Padre Island, a sandy barrier island on the lower coast; and (7) the sandy Brazos Island barrier peninsula and the Rio Grande fluvial and deltaic headland. Significant net shoreline advance occurred in more limited areas (1) adjacent to the jetties that protect dredged channels at Sabine Pass, Bolivar Roads, Aransas Pass, and Brazos Santiago Pass; (2) near tidal inlets at the western ends of Galveston Island and Matagorda Peninsula; (3) southwest of the mouth of the Brazos River; (4) along part of Matagorda Island; and (5) on central Padre Island.

Shoreline change rates measured for the most recent short-term period (2000 to 2019) are similar to those calculated for the longer period, averaging 1.25 m/yr (4.1 ft/yr) of net retreat. Long-term rates estimated from historical shoreline positions are significantly lower than late Pleistocene to early Holocene rates that range from 3 to 55 m/yr (8 to 181 ft/yr) estimated from bathymetric contour shoreline proxies and past sea-level positions, but are similar to mid- to late Holocene retreat rates of 0.1 to 1.7 m/yr (0.4 to 5.4 ft/yr). A statistical relationship between

postglacial relative sea-level rise rates and retreat rates calculated from the bathymetric shoreline proxy suggests that each millimeter per year of sea-level rise translates to 0.8 to 1.8 m/yr (3 to 6 ft/yr) of shoreline retreat. This relationship provides an empirical approach to estimating future shoreline retreat rates under sea-level rise scenarios that may be similar to those observed during postglacial sea-level rise.

Shoreline change rates were calculated using the latest coast-wide airborne lidar data and imagery acquired in spring 2019. Updated rates include the effects (erosion, deposition, and nearly two years of recovery) associated with Hurricane Harvey, which struck the middle Texas coast in August 2017 and strongly impacted beach and dune morphology from Mustang Island to the Brazos–Colorado headland.

# INTRODUCTION

The Texas coastal zone (fig. 1) is among the most dynamic geologic environments on earth. Shoreline position is a critical parameter that reflects the balance among several important processes, including sea-level rise, land subsidence, sediment influx, littoral drift, and storm frequency, intensity, and recovery. Because the Texas coast faces ongoing developmental pressures as the coastal population grows, an accurate and frequent analysis of shoreline movement serves as a planning tool to identify areas of habitat loss, better quantify threats to residential, industrial, and recreational facilities and transportation infrastructure, and help understand the natural and anthropogenic causes of shoreline movement.

The Texas Gulf shoreline forms the seaward boundary along a series of Holocene geomorphic features (fig. 1) that include barrier islands, strandplains, fluvial and deltaic headlands, and chenier plains (Aronow and others, 1982; Brown, Brewton, and McGowen, 1975; Brown and others, 1975, 1976; LeBlanc and Hodgson, 1959). Three major rivers, including the Brazos and Colorado on the upper (northeastern) Texas coast and the Rio Grande on the lower (southern) Texas coast, directly discharge into the Gulf of Mexico, although their contribution to the overall coastal sediment budget has diminished with the construction of dams for flood control, water supply, and recreation in each river basin in the 20th century. Coastal embayments such as Galveston Bay formed landward of the Holocene barrier islands and peninsulas in late Pleistocene river valleys submerged during the Holocene transgression (LeBlanc and Hodgson, 1959), and shore-parallel lagoons such as Laguna Madre and eastern Matagorda Bay formed as barrier islands and peninsulas aggraded and expanded laterally along the coast. Tidal exchange between the bays, lagoons, and the Gulf of Mexico occurs through tidal passes and channels at Sabine Pass, Rollover Pass (scheduled for closure in 2020), Bolivar Roads, San Luis Pass, Brown Cedar Cut, Pass Cavallo, Cedar Bayou, Aransas Pass, Packery Channel, Mansfield Channel, and Brazos Santiago Pass (fig. 1). Prevailing onshore, southeasterly winds generate littoral currents in the northwestern Gulf of Mexico that carry sediments toward a longshore

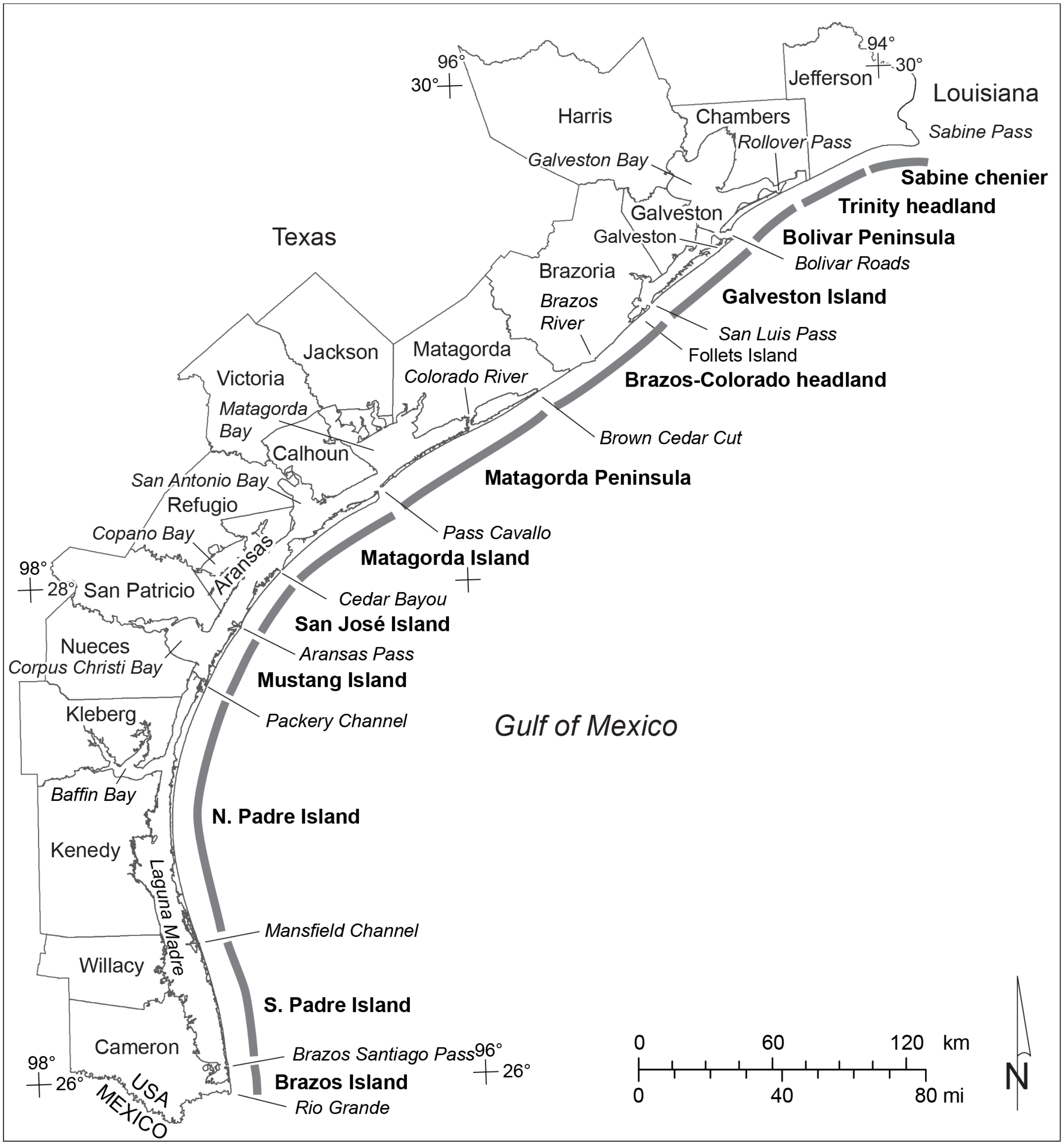


Figure 1. Map of the Texas coastal zone showing principal geomorphic features (bold) and coastal counties. Shaded segments parallel to the shoreline indicate the approximate extent of major barrier islands, peninsulas, fluvial and deltaic headlands, and strandplains.

convergence zone along Padre Island between the Rio Grande deltaic headland to the south and the Brazos–Colorado headland to the northeast. Similarly, a smaller convergence zone occupies the embayment between the Brazos–Colorado headland and the Trinity headland along the upper Texas coast.

The latest trends in shoreline change rates are a critical component in understanding the potential impact that sea level, subsidence, sediment supply, and coastal engineering projects have on the coastal population and sensitive coastal environments such as beaches, dunes, and wetlands. Rapidly eroding shorelines threaten habitat and recreational, residential, transportation, and industrial infrastructure and can also significantly increase the vulnerability of communities to tropical storms. Periodic analyses of shoreline position, rates of movement, and factors contributing to shoreline change give citizens, organizations, planners, and regulators an indication of expected future change and help determine whether those changes are accelerating, decelerating, or continuing at the same rate as past changes.

Historical change rates for the Texas Gulf shoreline were first determined by the Bureau of Economic Geology (Bureau) in the 1970s and presented in a series of publications separated at natural boundaries along the 590 km (367 mi) of shoreline (Morton, 1974, 1975, 1977; Morton and Pieper, 1975a, 1975b, 1976, 1977a, 1977b; Morton and others, 1976). This publication series presented net long-term change rates determined from shoreline positions documented on 1850 to 1882 topographic charts published by the U.S. Coast and Geodetic Survey (Shalowitz, 1964) and aerial photographs acquired between about 1930 and 1975. Rates of change for the entire Gulf shoreline were updated through 1982 based on aerial photographs (Paine and Morton, 1989; Morton and Paine, 1990). Updates for subsets of the Texas Gulf coast include the upper coast between Sabine Pass and the Brazos River through 1996 (Morton, 1997), the Brazos River to Pass Cavallo (Gibeaut and others, 2000) and Mustang and northern Padre Island through 2000 (Gibeaut and others, 2001). Shoreline positions in 2000–2001, established using an airborne lidar topographic mapping system, were used in Bureau studies and as part of a Gulf-wide assessment of shoreline change that included the Texas coast (Morton and others, 2004). Coast-wide rates of historical shoreline change were updated using 2007 aerial photographs, the most recent coast-wide coverage predating Hurricane Ike in 2008 (Paine and others, 2011, 2012). Short-term shoreline movement, and its relationship to long-term trends, was determined from annual shoreline positions extracted from airborne lidar surveys conducted in 2010, 2011, and 2012 (Paine and others, 2013, 2017). The most recent update to historical Texas Gulf shoreline change rates used shoreline positions extracted from the 2012 airborne lidar survey (Paine and others, 2014).

This report describes the 2019 update to long- and short-term shoreline movement rates that are published as a GIS data set and displayed online on the Bureau's interactive shoreline movement web viewer (https://coastal.beg.utexas.edu/shorelinechange2019/), the latest update to the Bureau's long-term Texas Shoreline Change Project series (http://www.beg.utexas.edu/research/programs/coastal/the-texas-shoreline-change-project). These rates were calculated from selected shoreline vintages that began in most areas with the 1930s aerial photographs and included ground-based GPS surveys conducted in select areas during the mid-1990s and coast-wide airborne lidar surveys acquired in 2000, 2012, and 2019. For the lidar surveys, we use a carefully chosen elevation contour extracted from digital elevation models (DEMs) as the shoreline proxy that best matches the wet-beach/dry-beach shoreline position interpreted from aerial photographs. For this most current shoreline change update, we used airborne lidar survey data acquired by the Bureau in April to June 2019. Shorelines extracted from the 2019 lidar data represent conditions 20 to 22 months after Hurricane Harvey, a major tropical cyclone that made landfall on the middle Texas coast in late August 2017. Tropical Storm Imelda made landfall in September 2019 after the 2019 lidar survey was completed and is not included in this analysis of shoreline movement.

## Relative Sea Level

Changes in sea level relative to the ground surface have long been recognized as a major contributor to shoreline change (*e.g.* Bruun, 1954, 1962, 1988; Cooper and Pilkey, 2004). Rising sea level inundates low-relief coastal lands causing shoreline retreat by submergence, and elevates dynamic coastal processes (currents and waves) that can accelerate shoreline retreat by physical erosion. Changes in relative sea level include both changes in the ocean-surface elevation ("eustatic" sea level) and changes in the elevation of the ground caused by subsidence or uplift. Eustatic sea-level change rates, established by monitoring average sea level at long-record tide gauge stations around the world and more recently using satellite altimetry, vary over a range of about 1 to 4 mm/yr. Gutenberg (1941) calculated a eustatic rate of 1.1 mm/yr from tide gauge data. Estimates based on tide gauge data since then have ranged from 1.0 to 1.7 mm/yr (Gornitz and others, 1982; Barnett, 1983; Gornitz and Lebedeff, 1987; Church and White, 2006), although Emery (1980) supported a higher global average of 3.0 mm/yr that is comparable to more recent globally averaged rates based on satellite altimetry. Attempts to remove postglacial isostatic uplift or subsidence and geographical bias from historical tide gauge records resulted in eustatic estimates as high as 2.4 mm/yr (Peltier and Tushingham, 1989). Recent studies that include satellite altimetry data acquired since 1993 indicate that global rates of sea-level rise average 2.8 mm/yr to 3.3 mm/yr with postglacial rebound removed (Cazenave and Nerem, 2004; Leuliette and Willis, 2011; Church and White, 2011; Church and others, 2013; Cazenave and others, 2014). Much of this recent rise is interpreted to result from thermal expansion of the oceans with a possible contribution from melting of glaciers and polar ice (Cazenave and Nerem, 2004; FitzGerald and others, 2008; Leuliette and Miller, 2009). The most recent analyses of satellite-based radar altimetry data interpret a 0.08 mm/yr$^2$ acceleration in sea-level rise rate since 1993 (Nerem and others, 2018).

In major sedimentary basins such as the northwestern Gulf of Mexico, eustatic sea level rise is exacerbated by subsidence. Published rates of relative sea-level rise measured at tide gauges along the Texas coast are higher than eustatic sea-level rates (Swanson and Thurlow, 1973; Lyles and others, 1988; Penland and Ramsey, 1990; Paine, 1991, 1993). The most recent relative sea-level rise rates from selected Texas tide gauges range from 3.60 to 6.55 mm/yr (fig. 2; table 1). These rates were calculated from data acquired by the National Oceanic and Atmospheric Administration through 2019 from periods of record that begin between 1904 (Galveston Pier 21) and 1983 (Corpus Christi). The highest rates (above 4 mm/yr) are calculated for upper and middle Texas coast tide gauges at Sabine Pass, Galveston, Freeport, Rockport, and Corpus Christi. The southernmost gauges have the lowest long-term rates of 3.60 at Port Mansfield and 4.10 mm/yr at Port Isabel.

Galveston Pier 21 has the longest period of record on the Texas coast. Long-term rate of sea-level rise calculated from monthly averages of sea level between 1904 and 2019 (fig. 3) is 6.55 mm/yr.

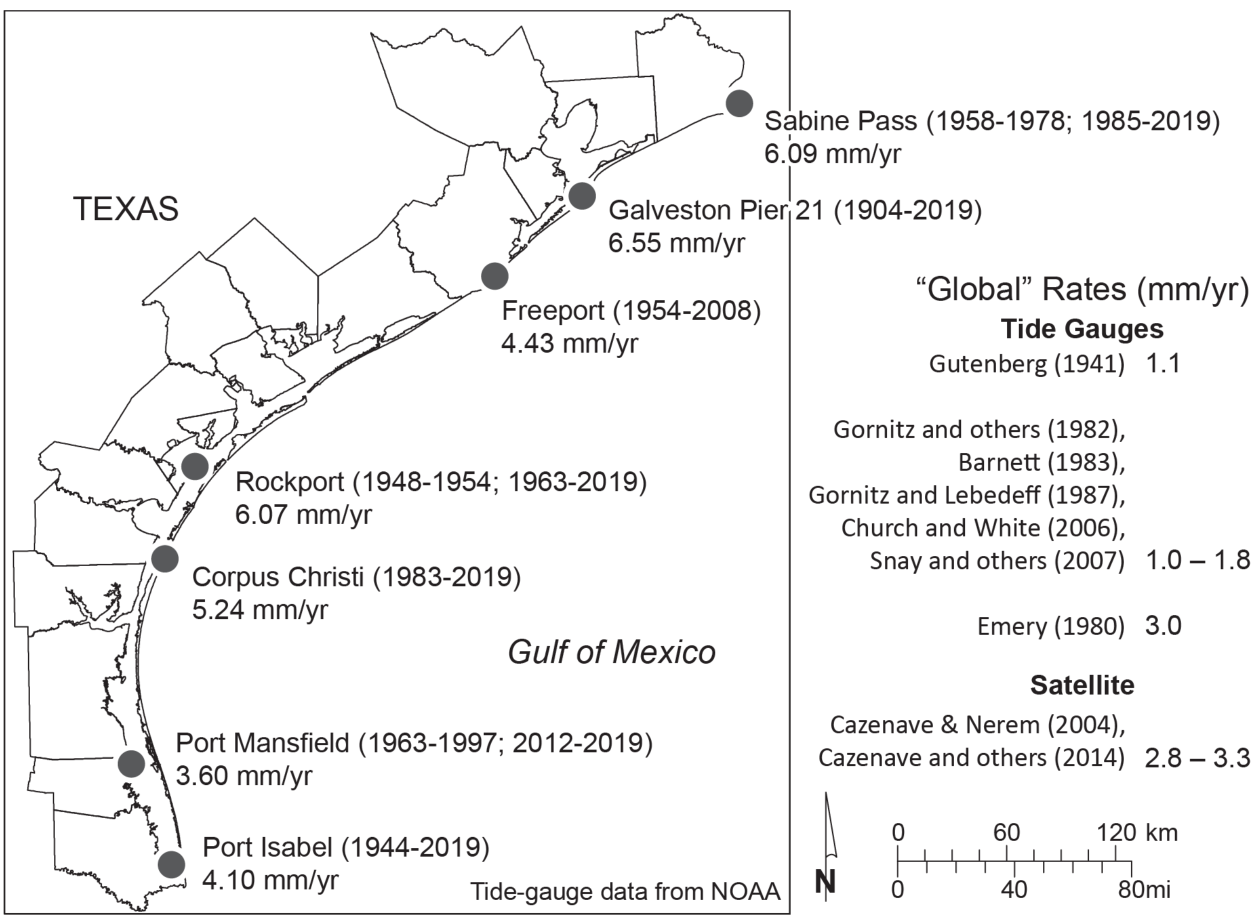


Figure 2. Sea-level trend at selected Texas tide gauges through 2019 and "global" rates determined from tide-gauge and satellite data. Texas tide-gauge data from National Oceanic and Atmospheric Administration.

Table 1. Long-term rates of relative sea-level rise at select Texas tide gauges (fig. 2) through 2018. Data from National Oceanic and Atmospheric Administration.

| **Tide gauge** | **Beginning year** | **Duration (yr)** | **Rate (mm/yr)** | **95% confidence interval (+/-, mm/yr)** |
|---|---|---|---|---|
| Sabine Pass | 1958 | 60 | 5.86 | 0.74 |
| Galveston Pier 21 | 1904 | 114 | 6.51 | 0.22 |
| Galveston Pleasure Pier (removed 2011) | 1957 | 54 | 6.62 | 0.69 |
| Freeport (removed 2008) | 1954 | 54 | 4.43 | 1.05 |
| Rockport | 1937 | 81 | 5.62 | 0.48 |
| Port Mansfield | 1963 | 55 | 3.19 | 0.73 |
| Padre Island (through 2006) | 1958 | 48 | 3.48 | 0.75 |
| Port Isabel | 1944 | 74 | 4.00 | 0.33 |

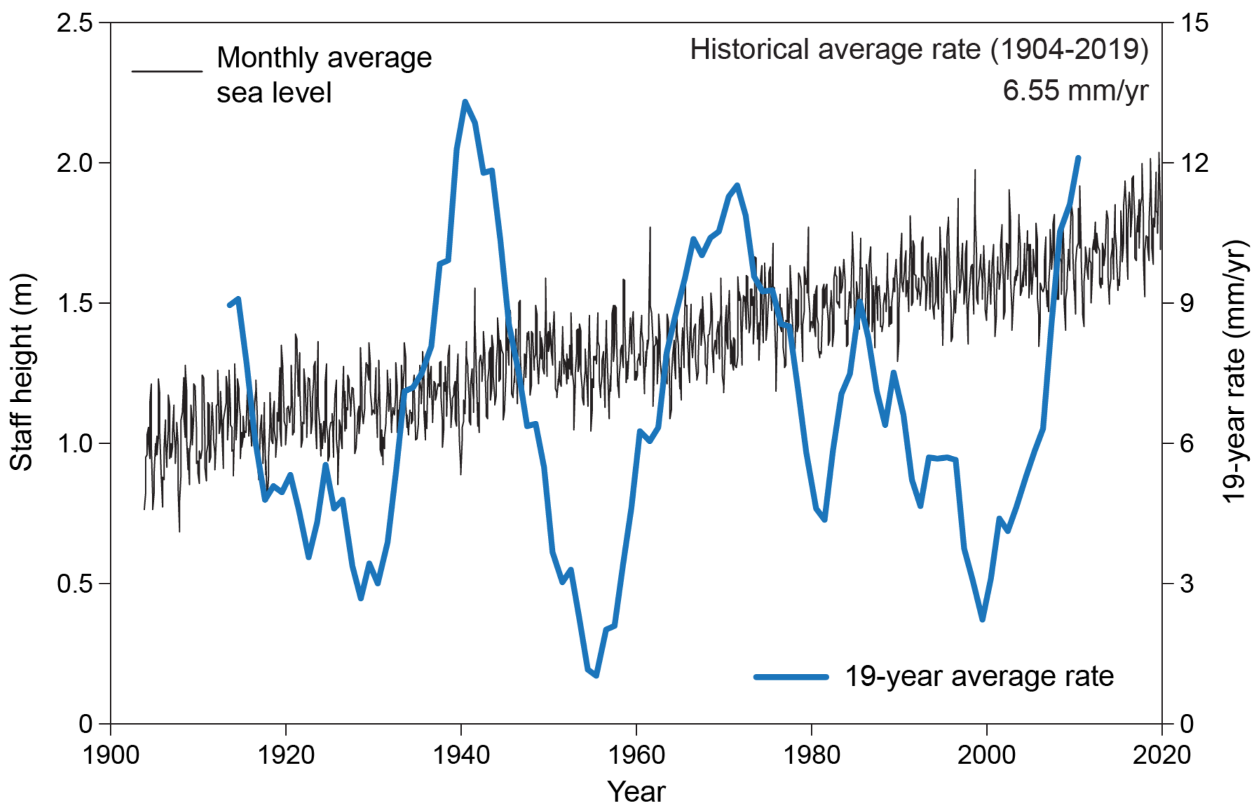


Figure 3. Sea-level trend at Galveston Pier 21, 1904 to 2019. Thin black line is monthly average sea level. Thick blue line is the average sea level change rate measured over a 19-year period (the tidal datum epoch) and plotted at the center date of the period. Data from National Oceanic and Atmospheric Administration.

Sea-level rise at this gauge has not been constant; calculations of average rate of change over a rolling 19-year window (chosen to match the duration of the 19-year National Tidal Datum Epoch and centered on the mid-date) show multiyear oscillations in average rate that range from 1.0 to 13.3 mm/yr (fig. 3). Most recently, average rates (since about 2000) have increased from 2.2 to 12.1 mm/yr.

Tide-gauge data represent single points along the coast and may not be representative of relative sea-level rise along the entire coast. Geodetic releveling data obtained from the National Geodetic Survey at benchmarks along the Texas coast from Galveston Bay to the Rio Grande show local variation in subsidence rates that would produce average rates of relative sea-level rise ranging from about 2 to more than 20 mm/yr. These rates are significantly higher than both the estimated long-term subsidence rate of 0.05 mm/yr or less since the last interglacial at about 100 ka (Paine, 1993) and global sea-level rise estimates, but are lower than average rates of postglacial sea-level rise during the early to middle Holocene (Shepard, 1960; Balsillie and Donoghue, 2004; Milliken and others, 2008; Paine and others, 2012). Despite the wide range in estimated subsidence rates, most of the rates fall within the range observed for the long-term Texas tide gauges, suggesting that the gauges are representative regional indicators of relative sea-level rise.

## Tropical Cyclones

There are numerous examples of the significant impact that tropical cyclones (tropical storms and hurricanes) have on the Texas Gulf shoreline (*e.g.* Price, 1956; Hayes, 1967; Morton and Paine, 1985). Cyclones include tropical storms (sustained winds between 62 and 118 km/hr, or 39 and 73 mi/hr) and hurricanes that are classified following the Saffir/Simpson system (Simpson and Riehl, 1981). Category 1 hurricanes have sustained winds of 119 to 153 km/hr (74 to 95 mi/hr); Category 2: 154 to 177 km/hr (96 to 110 mi/hr); Category 3: 178 to 208 km/hr (111to 129 mi/hr); Category 4: 209 to 251 km/hr (130 to 156 mi/hr); and Category 5: greater than 252 km/hr (157 mi/hr). In general, minimum central pressure decreases and pressure- and wind-driven storm surge increases as the categories increase. Two critical parameters that influence the erosion potential of a tropical cyclone are surge height and surge duration: the longer sea level is elevated above normal during storm passage, the greater the potential for redistribution of sediment eroded from the beach. Beach and dune recovery after storm passage follows several distinct stages and can extend beyond two years after storm landfall (Morton and Paine, 1985; Morton and others, 1994). The ending date (2019) for this update of shoreline change rates allowed nearly eleven years for recovery from Hurricane Ike (2008), which was a large Category 2 storm that severely eroded upper Texas coast beaches and dunes, and nearly two years for recovery from Hurricane Harvey (2017), a Category 4 storm that made landfall on the middle Texas coast. Tropical Storm Imelda made landfall near Freeport in September 2019, three months after the 2019 airborne lidar survey was completed for this update.

Historical lists (Roth, 2010) and records maintained by the National Oceanic and Atmospheric Administration indicate that 65 hurricanes and 62 tropical storms have struck the Texas coast from 1850 through 2019. On average, four hurricanes and four tropical storms make landfall in Texas per decade. The longest hurricane-free period in Texas extended nearly 10 years from October 1989 to August 1999 (Roth, 2010).

From 1990 through 2018, the period most applicable to this update (Tropical Storm Imelda made landfall in September 2019, after the 2019 lidar survey), 21 tropical cyclones crossed the Texas coast (table 2). Included are 14 tropical storms and 7 hurricanes that ranged in strength from Category 1 to Category 4 at landfall. Only 1 hurricane and 4 tropical storms affected Texas during the 1990s. From 2000 to 2018, there were 6 hurricanes and 10 tropical storms, a combined cyclone frequency that is slightly higher than the historical average. Storm frequency was higher between 2000 and 2009 (5 hurricanes and 6 tropical storms) than it was between 2010 and 2018 (1 hurricane and 4 tropical storms). The most severe storms in the last two decades were Hurricanes Bret, Rita, Ike, and Harvey. Hurricane Bret was a former Category 4 storm that weakened before landfall on Padre Island in August 1999. Hurricane Rita was

Table 2. Tropical cyclones affecting the Texas coast since 1990. TD = tropical depression; TS = tropical storm; H = hurricane; number following H designates numeric strength according to the Saffir/Simpson scale (Simpson and Riehl, 1981). Data from the National Oceanic and Atmospheric Administration and Roth (2010).

| Year | Category | Name | Begin date | End date | Landfall |
|---|---|---|---|---|---|
| 1993 | TS | Arlene | 6/18/1993 | 6/21/1993 | Northern Padre Island |
| 1995 | TS | Dean | 7/28/1995 | 8/2/1995 | Freeport |
| 1998 | TS | Charley | 8/21/1998 | 8/24/1998 | Aransas Pass |
| 1998 | TS | Frances | 9/8/1998 | 9/13/1998 | Matagorda Island |
| 1999 | H4 | Bret | 8/18/1999 | 8/25/1999 | Padre Island (weakened) |
| 2001 | TS | Allison | 6/5/2001 | 6/17/2001 | Freeport |
| 2002 | TS | Bertha | 8/4/2002 | 8/9/2002 | Northern Padre Island |
| 2002 | TS | Fay | 9/5/2002 | 9/8/2002 | Matagorda Peninsula |
| 2003 | H1 | Claudette | 7/8/2003 | 7/17/2003 | Matagorda Peninsula |
| 2003 | TS | Grace | 8/30/2003 | 9/2/2003 | Galveston Island |
| 2005 | H5 | Rita | 9/18/2005 | 9/26/2005 | Sabine Pass (H3 at landfall) |
| 2007 | TS | Erin | 8/15/2007 | 8/17/2007 | San José Island |
| 2007 | H1 | Humberto | 9/12/2007 | 9/14/2007 | Upper Texas coast |
| 2008 | H2 | Dolly | 7/20/2008 | 7/25/2008 | Southern Padre Island |
| 2008 | TS | Edouard | 8/3/2008 | 8/6/2008 | Upper Texas coast |
| 2008 | H4 | Ike | 9/1/2008 | 9/15/2008 | Galveston (H2 at landfall) |
| 2010 | TS | Hermine | 9/5/2010 | 9/9/2010 | Rio Grande area |
| 2011 | TS | Don | 7/27/2011 | 7/29/2011 | Baffin Bay area (TD at landfall) |
| 2015 | TS | Bill | 6/15/2015 | 6/16/2015 | Matagorda Island |
| 2017 | TS | Cindy | 6/20/2017 | 6/23/2017 | Port Arthur to Cameron, LA |
| 2017 | H4 | Harvey | 8/17/2017 | 9/1/2017 | Rockport area |
| 2019 | TS | Imelda | 9/17/2019 | 9/19/2019 | Freeport area |

a Category 5 storm that weakened to Category 3 before landfall in the Sabine Pass area in September 2005. Hurricane Ike was a Category 4 storm that weakened to a very large Category 2 storm before landfall in September 2008. It produced an unusually high and long-duration storm surge that heavily impacted upper Texas coast beaches. Hurricane Harvey rapidly intensified to Category 4 as it approached the middle Texas coast before making landfall near Rockport on August 25, 2017 (Blake and Zelinsky, 2018). Hurricane Harvey is the most recent storm prior to the shoreline position considered in this update, making landfall 20 to 22 months before the 2019 airborne lidar survey of the Texas Gulf shoreline.

## METHODS

Shoreline change rates were calculated after including the 2019 lidar- and imagery-derived shoreline position into the set of shoreline positions that has been used to determine long-term Texas Gulf shoreline change rates presented in the Bureau's shoreline change publication series. Shoreline vintages were selected for change-rate analysis to conform with shorelines chosen for earlier calculations of shoreline change rate and to result in reasonably regular intervals between shorelines along a given transect. Shoreline rates presented in the publications before 2000 were listed as net, or average, rates of change between two end-point dates (the net distance the shoreline moved divided by the elapsed time). More recently, rates have also been calculated using linear regression analysis of all included shoreline positions. In the 2019 update, we present both rates in the data files and on the web viewer, but discuss net values in this report for historical consistency. In most cases, these rates are similar and either rate could be used.

Shoreline change rates were calculated following several steps, including:

(1) importing the 2019 shoreline position (extracted as a carefully chosen elevation contour from a 1-m resolution digital elevation model constructed from high-resolution lidar data) into a geographic information system data base (ArcMap, v. 10.4);

(2) checking the consistency of the chosen elevation contour with the position of the wet- and dry-beach boundary as depicted on 2016 and 2018 National Agricultural Imagery Program (NAIP) georeferenced aerial photographs and 2019 Bureau aerial imagery;

(3) selecting the shoreline vintages to use in the calculation of change rates (table 3), which include the earliest photograph-derived shoreline from the 1930s Tobin aerial photographs along with geographically extensive coastal photography from the 1950s, 1960s, 1974, 1990s, and 2007; GPS-derived shoreline positions from 1996 and 1998; and shoreline positions from airborne lidar surveys conducted by the Bureau in 2000, 2012, and 2019;

Table 3. Shoreline source dates and types used to calculate shoreline movement rates for each major Gulf of Mexico coastal segment. The 1930s to 1991 shorelines were mapped on aerial photographs, optically transferred to paper topographic maps, and digitized into a GIS database. The 1995 and 2007 shorelines were digitized directly from georeferenced aerial photographs. The 1996 and 1998 shorelines were determined by ground GPS surveys. The 2000, 2012, and 2019 shorelines were extracted from airborne lidar surveys conducted by the Bureau. Shoreline segment locations are shown on fig. 1.

| Segment | 1930s | 1950s | 1960s | 1970s | 1990s | 2000s | 2010s |
|---|---|---|---|---|---|---|---|
| Sabine Pass to Rollover Pass | 1930 | 1955-56 | 1965 | 1974 | 1996 | 2000, 2007 | 2012, 2019 |
| Bolivar Peninsula | 1930 | 1956 | 1965 | 1974 | 1996 | 2000, 2007 | 2012, 2019 |
| Galveston Island | 1930, 1934 | 1956 | 1964-65 | 1970, 1974 | 1995, 1996 | 2000, 2007 | 2012, 2019 |
| Brazos–Colorado headland | 1930, 1934 | 1956 | 1965 | 1974 | 1991, 1995 | 2000, 2007 | 2012, 2019 |
| Matagorda Peninsula | 1937 | 1956 | 1965 | 1974 | 1991 | 2000, 2007 | 2012, 2019 |
| Matagorda Island | 1937 | 1956-57 | 1965 | 1974 | 1995 | 2000, 2007 | 2012, 2019 |
| San José Island | 1931, 1937 | 1957-58 | 1965 | 1974 | 1995, 1998 | 2000, 2007 | 2012, 2019 |
| Mustang Island | 1937 | 1958-59 | 1965, 1969 | 1974 | 1990, 1995 | 2000, 2007 | 2012, 2019 |
| N. Padre Island | 1937-38 | 1956, 1959-60 | 1969 | 1974-75 | 1990, 1995 | 2000, 2007 | 2012, 2019 |
| S. Padre Island | 1934, 1937 | | 1960, 1969 | 1974-75 | 1995 | 2000, 2007 | 2012, 2019 |
| Brazos Island | 1934, 1937 | | 1960 | 1974 | 1995 | 2000, 2007 | 2012, 2019 |

(4) creating shore-parallel baselines from which shore-perpendicular transects were cast at 50-m intervals along the shoreline using the GIS-based extension software Digital Shoreline Analysis System version 5.0 (DSAS; Himmelstoss and others, 2018);

(5) calculating rates of change and associated statistics for the long-term (1930s to 2019), medium-term (1950s to 2019) and most recent short-term (2000 to 2019) periods using the transect locations and the selected shorelines within DSAS; and

(6) determining the intersection of the transect lines with the 2019 shoreline and creating GIS shape files containing (a) the rates and statistics of shoreline change measurements and (b) the measurement transects bounded by the most landward and seaward historical shoreline position for each measurement site (the shoreline change envelope).

Rates were calculated as both net (average) rates and linear-regression rates. For consistency with previous studies, only net rates are discussed in this report and displayed graphically on the accompanying web viewer. For comparison purposes, both net rates and linear-regression rates (and coefficients of determination) are shown for web viewer queries and in the accompanying GIS data set. Where regression coefficients of determination are relatively high (closer to 1.0), rates calculated using the linear regression method reasonably express the movement of the shoreline. Where coefficients are low (closer to 0), regression rates do not reasonably reflect the movement of the shoreline, perhaps because of inconsistent movement rates over time, including possible reversals of movement direction. Net rates, calculated as the distance between the shoreline position at the end and beginning of the monitoring period, divided by elapsed time, are analyzed for multiple periods (1930s to 2019, 1950s to 2019, and 2000 to 2019) to examine potential changes in movement rates over time.

Shoreline positions extracted from 2019 lidar data were chosen and verified by visually comparing a range of shoreline proxy contour elevations with the wet- and dry-beach boundary as shown on georeferenced 2016 and 2018 NAIP aerial photographs and imagery acquired

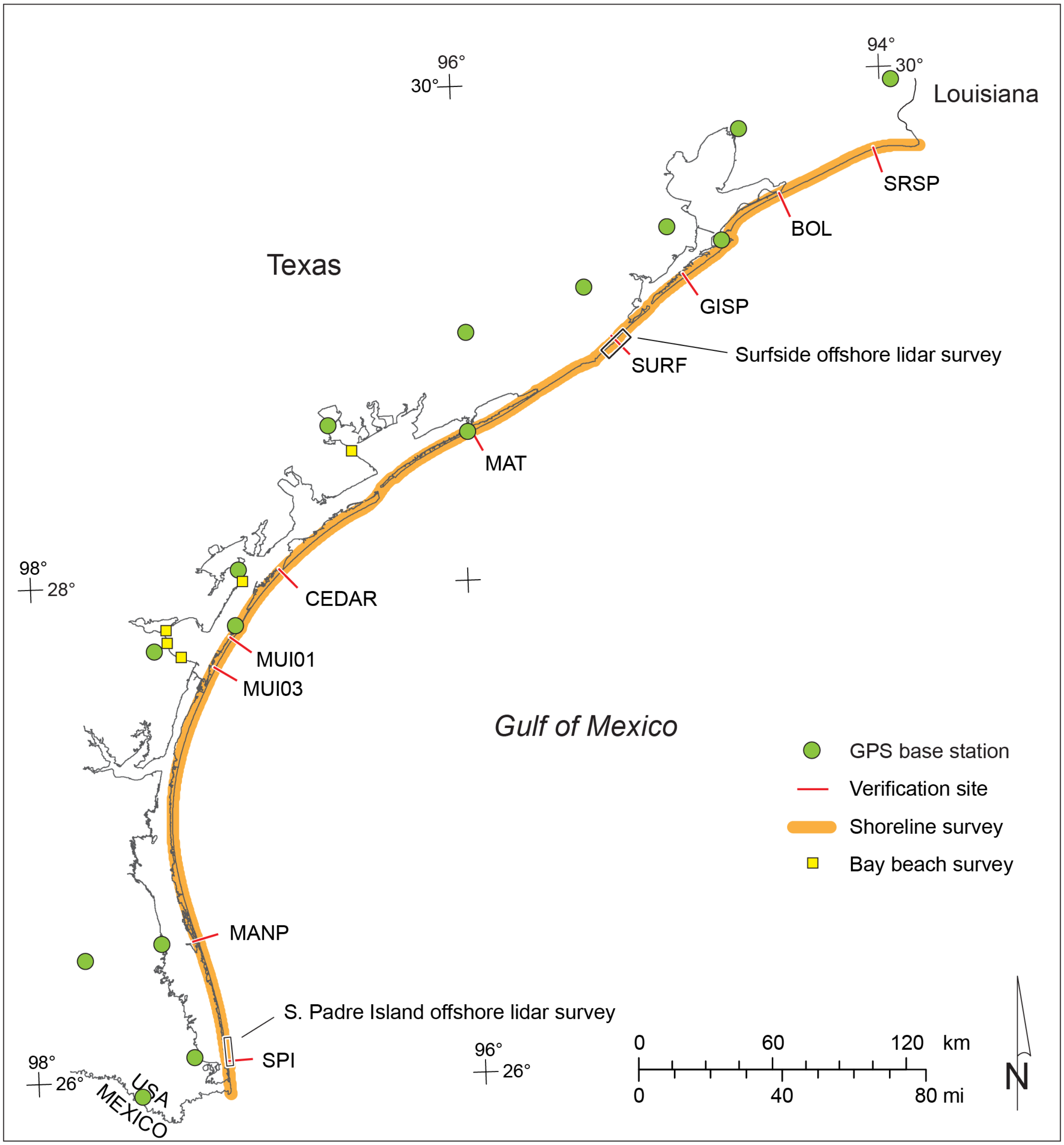


Figure 4. Location of 2019 Gulf shoreline, bay beach, and offshore lidar survey areas, ground GPS base stations, and shoreline position verification sites.

during the airborne survey. We also used beach profiles and GPS-mapped shorelines acquired for the Bureau's Texas High School Coastal Monitoring Program (THSCMP; Caudle and Paine, 2012, 2017) near the dates of the lidar survey to compare the observed wet-beach/dry-beach positions at representative long-term monitoring sites on Bolivar Peninsula, Galveston Island, Follets Island, Matagorda Peninsula, Mustang Island, and Padre Island (fig. 4).

## Sources of Shorelines

In general, the accuracy of the historical shoreline positions improves with advances in technology. There is some inherent uncertainty as to the precision of the data in the original topographic charts from the 1800s that were prepared by the U.S. Coast Survey. For aerial photography optical resolution, the quality of photographic negatives or digital images, mosaic compilation techniques, and georeferencing accuracy all improved over time between the earliest photographs in the 1930s and the most recent photographs (2007) used in this study. Another potential error is the position of the land-water interface (most consistently expressed as the wet-beach/dry-beach boundary) on aerial imagery. This position depends on the tidal cycle, beach slope, and wind direction, speed, and duration when the image was taken, and can differ according to date and location. For this update, the 1800s shorelines are considered to be the largest source of error and were not used in the calculation of shoreline movement.

As documented in previous Bureau publications, mapped shorelines from the 1800s to early 1990s were originally optically transferred to common paper 7.5-minute topographic base maps. The 1995 shoreline was digitized directly from georeferenced aerial imagery. The 1996 (upper coast) and 1998 (middle coast) shorelines were surveyed using differentially corrected GPS data acquired from a GPS receiver mounted on a motorized vehicle (Morton and others, 1993; Morton, 1997). The 2000 and 2012 shorelines were surveyed using an Optech ALTM 1225 airborne laser terrain mapping instrument (lidar). Laser range data were combined with differentially corrected aircraft position determined from GPS and an inertial measurement unit to determine land-surface position and elevation. Shoreline position was extracted from the lidar-derived digital elevation model at an elevation of 0.6 m (2.0 ft) above mean sea level (msl), which was determined to be the best match to the wet-beach/dry-beach boundary for those surveys. The 2007 shoreline was mapped within a GIS environment by digitizing the wet-beach/dry-beach boundary as depicted on high-resolution, georeferenced aerial photographs taken in 2007 (Paine and others, 2011).

Studies conducted when the Bureau began to use lidar data for shoreline position extraction, based on lidar data acquired in 2000 and 2001 and beach profiles acquired in 2001, determined that the wet-beach/dry-beach boundary occurred at 0.6 m msl (Gibeaut and others, 2000, 2001, 2002; Gibeaut and Caudle, 2009). Using the most seaward, continuous contour of 0.6 m msl provided a consistent shoreline proxy feature between the lidar datasets and historical mapping practices. During lidar data processing, the elevation values expressed as height above an ellipsoid (HAE) are transformed to North American Vertical Datum of 1988 (NAVD88) orthometric heights by applying a geoid model correction. Lidar datasets acquired by the Bureau between 2000 and 2012 used the National Geodetic Survey's (NGS) Geoid99 model to make the transformation from ellipsoidal heights to NAVD88 elevations. A mean sea-level correction was also applied before extracting the shoreline from the lidar datasets. Geoid99 has been superseded by newer geoid models as the NGS produces new geoid models every few years to more accurately represent the equipotential surface and incorporate additional data. Lidar surveys conducted since 2012 use the Geoid12B model to convert elevation values from HAE to elevations with respect to NAVD88, which may cause apparent differences in elevation between surveys. In addition, mean sea level continues to rise relative to NAVD88 (fig. 2 and table 1).

Before 2013, the 0.6 m msl elevation was used as the shoreline proxy from Bureau lidar-derived digital elevation models created using the Geoid99 model. This contour reasonably matched the position of the wet-beach/dry-beach boundary used as a mappable shoreline proxy on aerial imagery for the 2012 airborne lidar survey (Paine and Caudle, 2014). For the 2013 South Padre Island survey (Caudle and others, 2014, 2019), the 0.6 m msl elevation, with HAE transformed to NAVD88 elevations using the newer Geoid12B model, was too low on the shoreface and was discontinuous due to its proximity to the seaward edge of the topographic DEM, indicating the 0.6 m msl elevation was at or below the waterline in places. Beach profiles collected by Bureau staff and Texas High School Coastal Monitoring Program (THSCMP) students between 2000 and 2013, GPS-based shoreline mapping conducted by THSCMP students near the dates of the lidar survey, and comparisons with the position of the wet-beach/dry-beach boundary on aerial imagery acquired during the lidar survey were used to select a proxy elevation of 0.9 m msl that better matched the wet-beach/dry-beach boundary for that area and survey.

The process of rigorously evaluating the shoreline proxy elevation that best matches the wet-beach/dry-beach boundary includes comparing extracted elevation contours with the wet-beach/dry-beach position as expressed on aerial imagery, beach profiles, and the ground-based GPS-mapping relevant to each lidar survey. A similar evaluation process was conducted for the 2016 U. S. Army Corps of Engineers (USACE) and the 2017 post-Harvey lidar surveys.

The 2019 shoreline position was extracted from lidar data acquired by the Bureau between April 2 and June 2 (Appendix). Laser-range data were combined with aircraft position and orientation determined from ground- and aircraft-based GPS and an inertial measurement unit to determine land-surface position and height above the GRS80 ellipsoid. The Geiod12B model was applied to convert elevation values from HAE to elevations with respect to NAVD88.

To determine the shoreline proxy elevation that best matches the wet-beach/dry-beach boundary at the time of the survey, we examined (1) the 2019 Bureau lidar data and aerial imagery; (2) Gulf shoreline (Sargent Beach to Aransas Pass) lidar data collected by the Bureau in 2013, 2014, and 2015 (Paine and others, 2016); (3) the 2016 lidar data acquired by the USACE (USACE, 2017); (4) beach profiles collected by Bureau researchers and students participating in the THSCMP; (5) GPS-based shoreline mapping conducted by THSCMP students; and (6) the 2016 and 2018 NAIP aerial imagery. Through analysis of wet-beach/dry-beach boundary elevations reported in Bureau- and THSCMP-collected beach profiles (1997-2019), several elevation contours were examined to determine the elevation that best represents the shoreline position most consistent with historical mapping practices. A final shoreline position was extracted from the lidar-derived DEM at an elevation of 1.15 m (3.8 ft) NAVD88, which is equivalent to approximately 1 m (3.3 ft) msl.

The extracted elevation contour should be reevaluated with each lidar survey to ensure that the shoreline proxy represents the best approximation of the wet-beach/dry-beach boundary at the time of the survey and not necessarily the elevation that was used during a previous survey. This approach ensures that the extracted elevation best represents current conditions and remains consistent with historical mapping of the shoreline position using the wet-beach/dry-beach boundary as depicted on aerial photographs.

## Positional Verification

The georeferencing of shoreline position is one of the principal sources of potential error in determining long-term shoreline change rates (Anders and Byrnes, 1991; Crowell and others, 1991; Moore, 2000). Georeferencing of the 2019 airborne lidar survey data was checked by (a) comparing ground GPS-derived and lidar-derived locations and elevations at Bureau-surveyed calibration targets and (b) comparing equivalent natural and constructed features common to 2019 airborne lidar survey data and georeferenced NAIP photographs taken in 2016 and 2018.

A third positional check, which addressed the relative position of the shoreline proxy (1.0 m [3.3 ft] msl elevation contour) and the wet-beach/dry-beach boundary, was accomplished by superimposing the lidar-derived shoreline proxy and GPS-based, wet-beach/dry-beach boundary data acquired in spring 2019 by Bureau researchers and THSCMP students on georeferenced 2016 and 2018 NAIP imagery. On Matagorda Peninsula, the wet-beach/dry-beach boundary was mapped by THSCMP participants in September 2018 and 2019. These comparisons, in some cases from imagery and ground-based GPS data acquired within a few days or weeks of the lidar survey date, generally showed good agreement (within a few meters) between boundaries interpreted from imagery and ground-based data and those extracted from lidar data. Minor differences (less than 10 m) in the position of the lidar-derived shoreline and the wet-beach/dry-beach boundary are likely to reflect real differences in beach morphology between the dates of the lidar survey and those of the imagery and ground-based GPS surveys in the highly dynamic, low-slope beach environment.

Comparisons of lidar-extracted shoreline and wet-beach/dry-beach positions were conducted for THSCMP beach profile sites at Bolivar Peninsula, Galveston Island State Park, Matagorda Peninsula, Mustang Island, and northern and southern Padre Island (fig. 4). On Bolivar Peninsula (fig. 5) there is good agreement among the wet-beach/dry-beach boundary surveyed by THSCMP students and Bureau staff near profile site BOL03 on April 23, 2019, the 2019 lidar-extracted shoreline, 2019 Bureau aerial imagery, and 2018 NAIP imagery. The GPS-mapped wet beach/

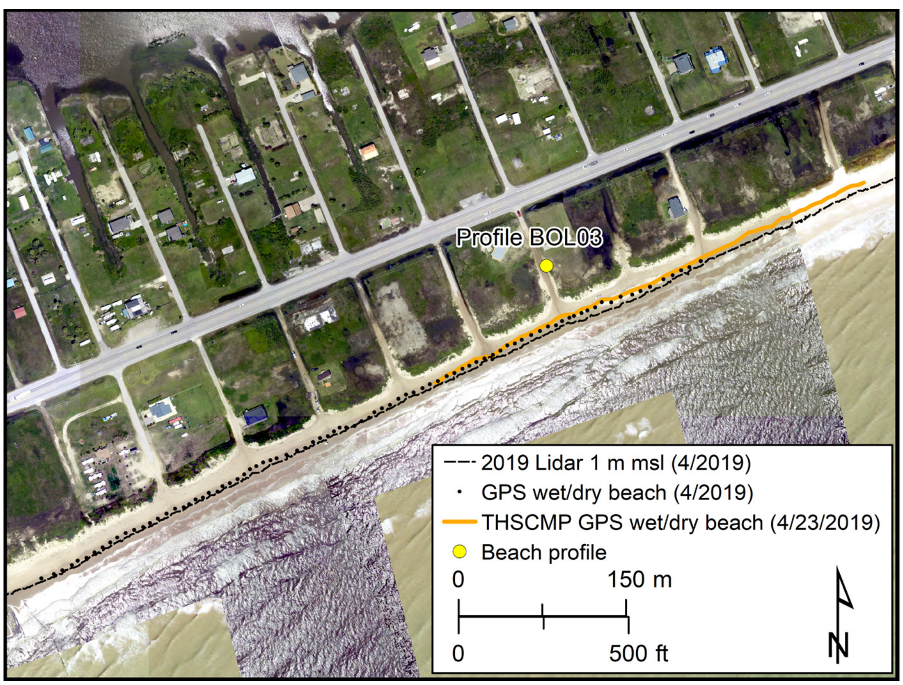


Figure 5. Shoreline position comparison at Bolivar Peninsula profile BOL03 near Rollover Pass (profile site BOL, fig. 4). Shorelines include the wet-beach/dry-beach boundary mapped on April 24, 2019 by THSCMP participants using ground GPS and the 1 m (3.3 ft) msl shoreline proxy extracted from airborne lidar data acquired in spring 2019, superimposed on 2018 NAIP and 2019 Bureau imagery. The NAIP imagery can be seen in the northeastern corner of the image.

dry beach boundary is at a higher elevation (0.05 to 0.15 m) on the beach and is 3 to 10 m farther landward.

At Galveston Island State Park (figs. 4 and 6), there is good agreement between the 2019 lidar-derived shoreline and the GPS-based wet-beach/dry-beach boundary mapped on April 10, 2019 (Bureau) and April 25, 2019 (THSCMP) at station BEG02. The lidar-derived shoreline proxy at 1 m (3.3 ft) msl is slightly higher (more landward) than the boundary between the wet and dry beach evident on the 2018 NAIP imagery, but coincides with the 2019 Bureau-acquired aerial imagery.

At Surfside Beach (figs. 4 and 7), there is excellent positional agreement between the 2019 lidar-derived shoreline proxy, the wet-beach/dry-beach boundary mapped on April 24, 2019 by

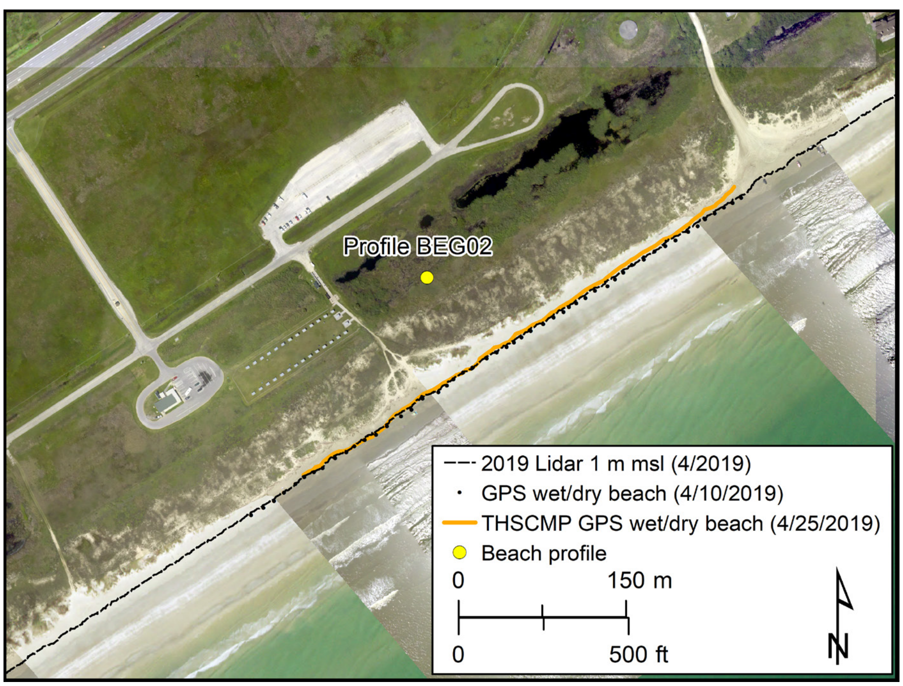


Figure 6. Shoreline position comparison at Galveston Island State Park site BEG02 (profile site GISP, fig. 4). Shorelines include the wet-beach/dry-beach boundary mapped on April 25, 2019 by THSCMP students and April 10, 2019 by Bureau staff using ground GPS and the 1 m (3.3 ft) msl shoreline proxy extracted from airborne lidar data acquired in spring 2019, superimposed on 2018 NAIP and 2019 Bureau imagery. NAIP imagery fills gaps in the Bureau imagery.

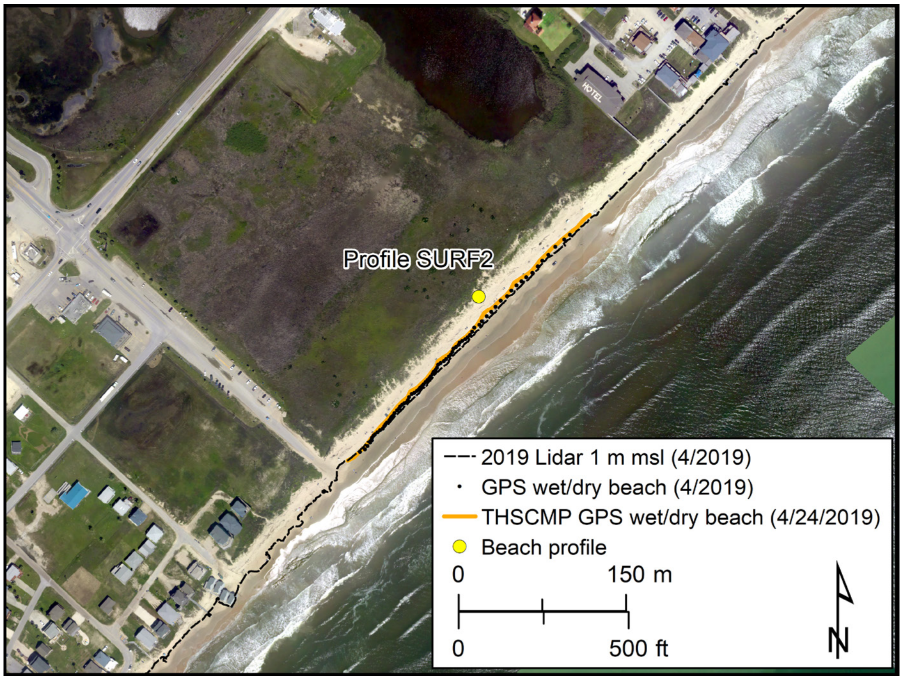


Figure 7. Shoreline position comparison at Surfside Beach site SURF2 (profile site SURF, fig. 4). Shorelines include the wet-beach/dry-beach boundary mapped on April 24, 2019 by THSCMP students and Bureau staff using ground GPS and the 1 m (3.3 ft) msl shoreline proxy extracted from airborne lidar data acquired in spring 2019, superimposed on 2019 Bureau imagery.

THSCMP participants and Bureau staff, and the 2019 aerial imagery. The lidar-derived shoreline position also coincides with the visual wet-beach/dry-beach boundary on the 2018 NAIP imagery.

On Matagorda Peninsula (site MAT02, figs. 4 and 8), there is good agreement between the lidar-extracted shoreline from the 2019 survey and the position of the wet-beach/dry-beach boundary mapped by THSCMP students on September 27, 2018. A THSCMP GPS-based survey of the wet-beach/dry-beach boundary acquired on September 25, 2019 and the visual wet-beach/dry-beach boundary on the 2019 Bureau aerial photography is slightly landward of the lidar-derived shoreline.

Lidar, imagery, and GPS comparisons on Mustang Island (sites MUI01 and MUI03, figs. 4 and 9) show good agreement between the lidar-extracted shoreline from the 2019 survey and

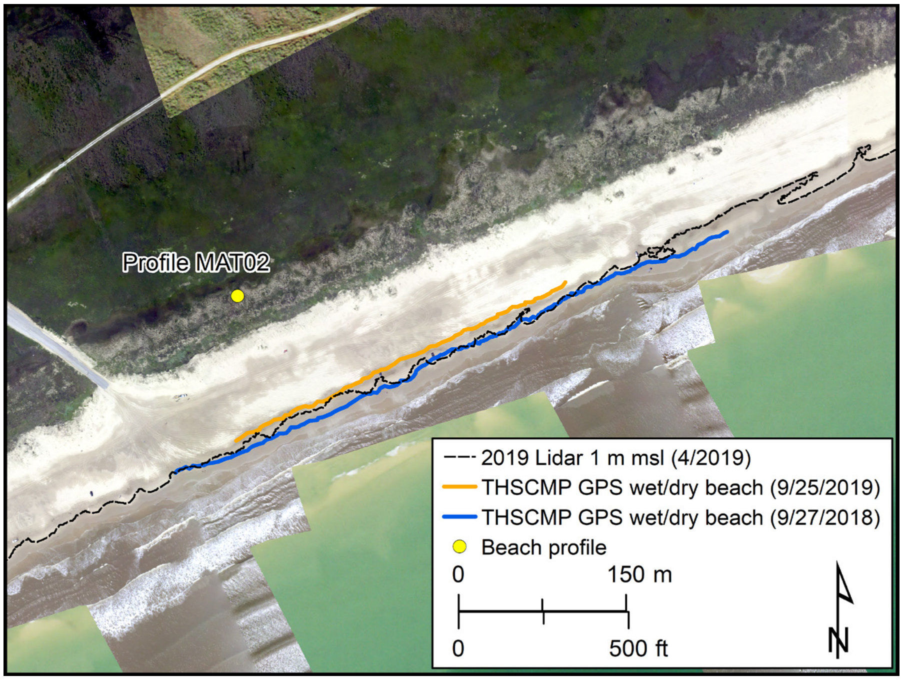

Figure 8. Shoreline position comparison at Matagorda Peninsula site MAT02 (profile site MAT, fig. 4). Shorelines include the wet-beach/dry-beach boundary mapped on September 27, 2018 and September 25, 2019 by THSCMP students using ground GPS and the 1 m (3.3 ft) msl shoreline proxy extracted from airborne lidar data acquired in spring 2019, superimposed on 2018 NAIP and 2019 Bureau imagery. NAIP imagery fills gaps in the Bureau imagery.

the wet-beach/dry-beach boundary evident on 2018 NAIP imagery and 2019 Bureau imagery. GPS surveys of the shoreline acquired by THSCMP students and the Bureau on April 30, 2019 indicates a shoreline position that coincides with the lidar-extracted shoreline.

On southern Padre Island (site SPI01, figs. 4 and 10), there is excellent positional agreement between the 2019 lidar-extracted shoreline and the wet-beach/dry-beach boundary as depicted on the 2018 NAIP aerial imagery. A GPS survey by THSCMP students and Bureau staff on January 10, 2019 shows good positional agreement between the wet-beach/dry-beach boundary and the lidar-derived shoreline.

We compared lidar-extracted shoreline positions to imagery at other coastal sites where beach surveys were not available. Minor differences between the lidar-derived shoreline and the visual

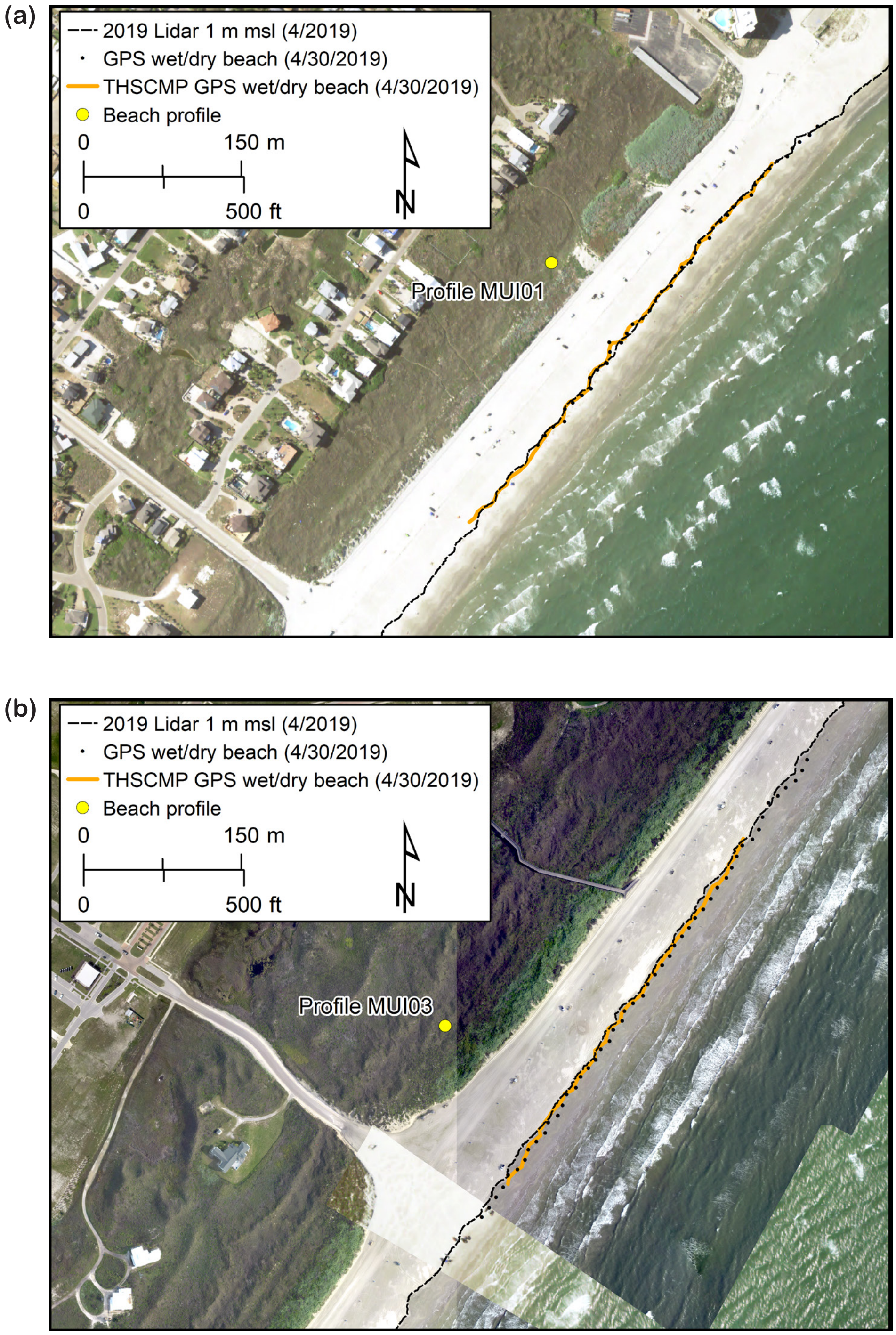


Figure 9. Shoreline position comparison at Mustang Island sites (a) MUI01 and (b) MUI03 (fig. 4). Shorelines include the wet-beach/dry-beach boundary mapped on April 30, 2019 by THSCMP students and Bureau staff using ground GPS and the 1 m (3.3 ft) msl shoreline proxy extracted from airborne lidar data acquired in spring 2019, superimposed on 2018 NAIP and 2019 Bureau imagery. NAIP imagery fills gaps in the Bureau imagery. MUI01 is shown on NAIP imagery only.

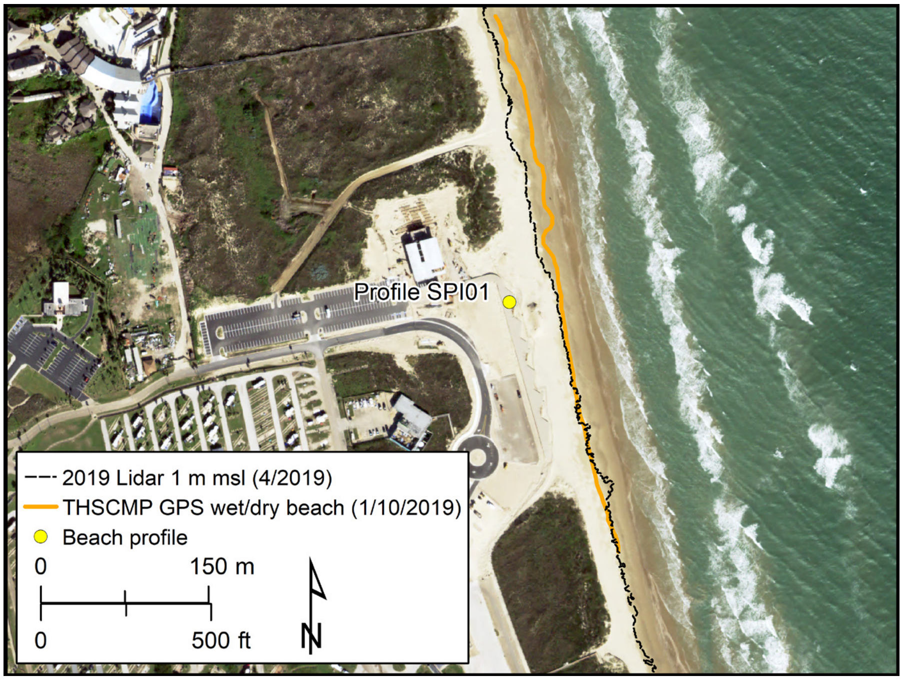

Figure 10. Shoreline position comparison on southern Padre Island at site SPI (fig. 4). Shorelines include the wet-beach/dry-beach boundary mapped on January 10, 2019 by THSCMP students and Bureau staff using ground GPS and the 1 m (3.3 ft) msl shoreline proxy extracted from airborne lidar data acquired in spring 2019, superimposed on 2018 NAIP imagery.

wet-beach/dry-beach boundary can be expected due to variations in the shoreface between the time of the imagery and lidar survey. Examples of these comparisons are located on the upper Texas coast at Sea Rim State Park (site SRSP, fig. 4), the middle Texas coast at Cedar Bayou between San José and Matagorda Islands (site CEDAR, fig. 4), and the lower Texas coast adjacent to Mansfield Pass on Padre Island (site MANP, fig. 4). At Sea Rim State Park (fig. 11) and Cedar Bayou (fig. 12), the extracted 1-m (3-ft) shoreline determined from airborne lidar data coincides well with the wet-beach/dry-beach boundary depicted on the 2019 Bureau imagery. Although not shown, the lidar-derived shoreline at Cedar Bayou closely coincides with the wet-beach/dry-beach boundary depicted on 2018 NAIP aerial imagery. On Padre Island near Mansfield Pass, agreement is good between lidar-derived shoreline position and the wet-beach/dry-beach boundary on the 2018 NAIP imagery (fig. 13). Similar reasonable agreement between

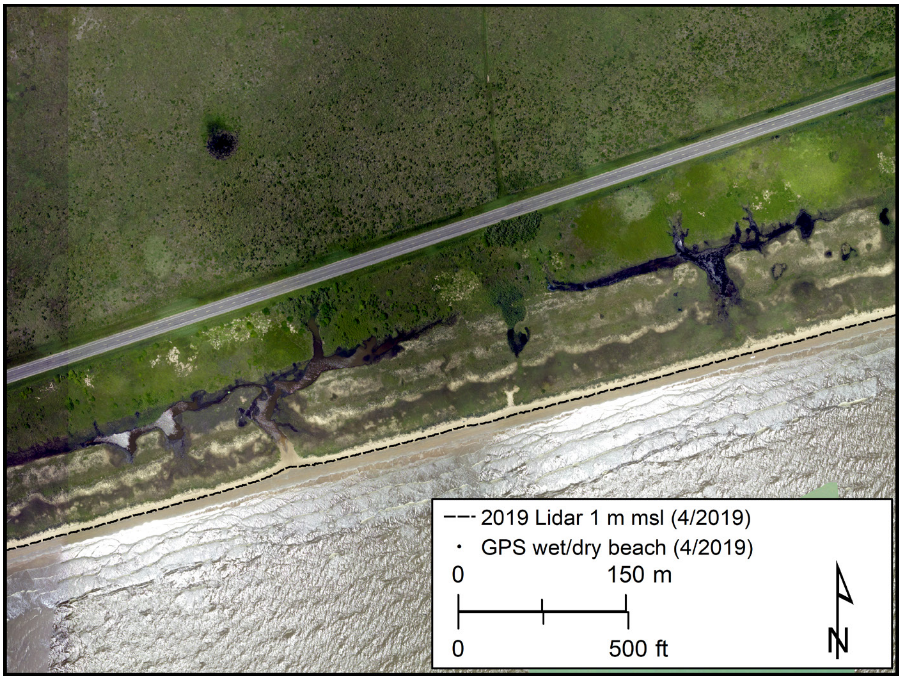

Figure 11. Shoreline position comparison on the upper Texas coast at Sea Rim State Park (SRSP, fig. 4). The 1 m (3.3 ft) msl shoreline proxy extracted from spring 2019 lidar data is superimposed on 2019 Bureau imagery.

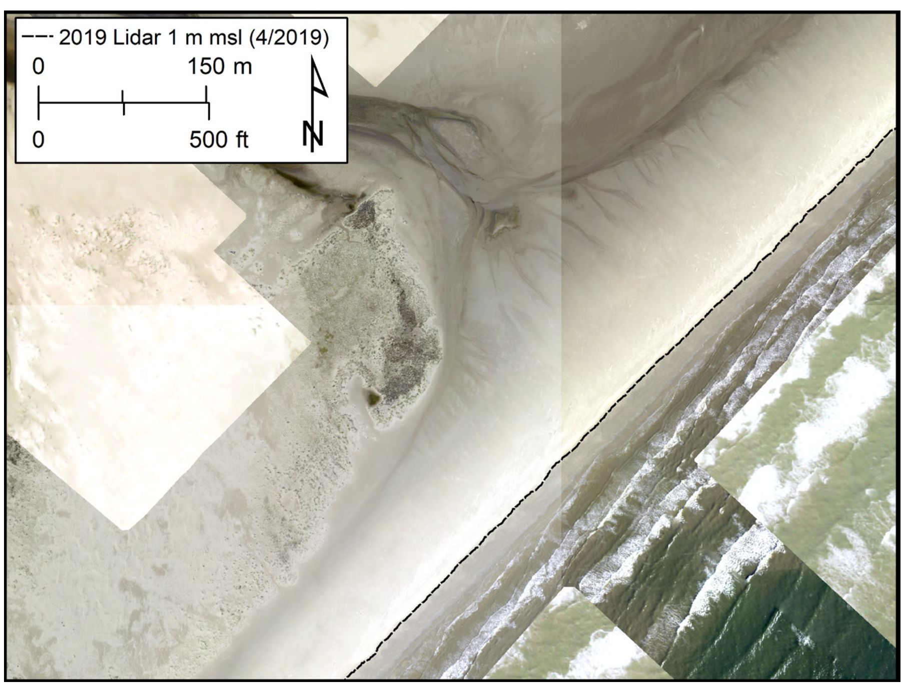

Figure 12. Shoreline position comparison at Cedar Bayou on the middle Texas coast (site CEDAR, fig. 4). The 1 m (3.3 ft) msl shoreline proxy extracted from spring 2019 lidar data is superimposed on 2019 Bureau imagery.

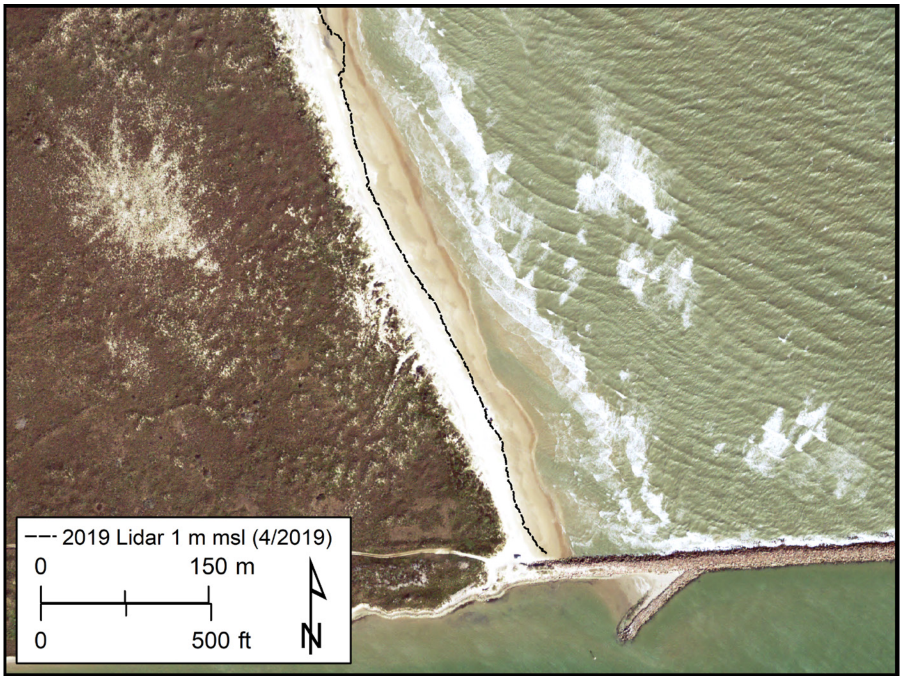

Figure 13. Shoreline position comparison on the lower Texas coast at Mansfield Pass (site MANP, fig. 4). The 1 m (3.3 ft) msl shoreline proxy extracted from spring 2019 lidar data is superimposed on 2018 NAIP imagery.

lidar-extracted shoreline position and shoreline features depicted on aerial imagery acquired in 2016, 2018, and 2019 was observed along all major segments of the Texas coast.

## TEXAS GULF SHORELINE CHANGE THROUGH 2019

Rates of long-term Gulf shoreline change, calculated from shoreline positions between the 1930s and 2019 (fig. 14; table 4), averaged 1.27 m/yr (4.17 ft/yr) of retreat for net-rate and 1.29 m/yr (4.23 ft/yr) for linear regression-rate calculations. Rates were calculated at 11,722 sites along the entire Texas coast spaced at 50 m (164 ft). Net retreat occurred at 9,336 sites (80 percent) and advance occurred at 2,225 sites (19 percent). No significant net movement was determined at the remaining sites. Net retreat at rates greater than 0.6 m/yr (2.0 ft/yr) was measured at 7,043 sites (60 percent). The average movement rate is slightly higher than the average movement rate of 1.26 m/yr (4.13 ft/yr) determined for the most recent previous update through 2012 (Paine and others, 2014). Shorelines along the northeastern Texas coast (from Sabine Pass to the mouth of the Colorado River) generally retreated at greater rates than those on the middle and lower coast. Average change rates were retreat at 1.71 m/yr (5.6 ft/yr) for the northeastern part of the coast and retreat at 0.97 m/yr (3.2 ft/yr) for the middle and lower coast.

From the upper coast to the lower coast, notable extensive areas of relatively high long-term retreat rates include the Sabine chenier and Trinity headland area, an area on Galveston Island west of the seawall, Follets Island near San Luis Pass, the fluvial and deltaic headland of the Brazos and Colorado rivers, Matagorda Peninsula west of the Colorado River, Matagorda Peninsula and Matagorda Island near Pass Cavallo, northern San José Island, northern Padre Island, and most of the southern half of Padre Island (fig. 14). Limited areas of general net shoreline advance are found on the upper coast near the Sabine Pass and Bolivar Roads jetties, at the western tip of Galveston Island, adjacent to the mouth of the Brazos River, at the western end of Matagorda Peninsula, on the middle Texas coast along the northern part of Matagorda Island and near Aransas Pass, and on Padre Island near Baffin Bay and the southern end of the island (fig. 14).

Closely spaced measurement sites allow estimates of land loss to be made (fig. 14 and table 4). The annual rate of land loss along the Texas Gulf shoreline, updated from the 1930s through

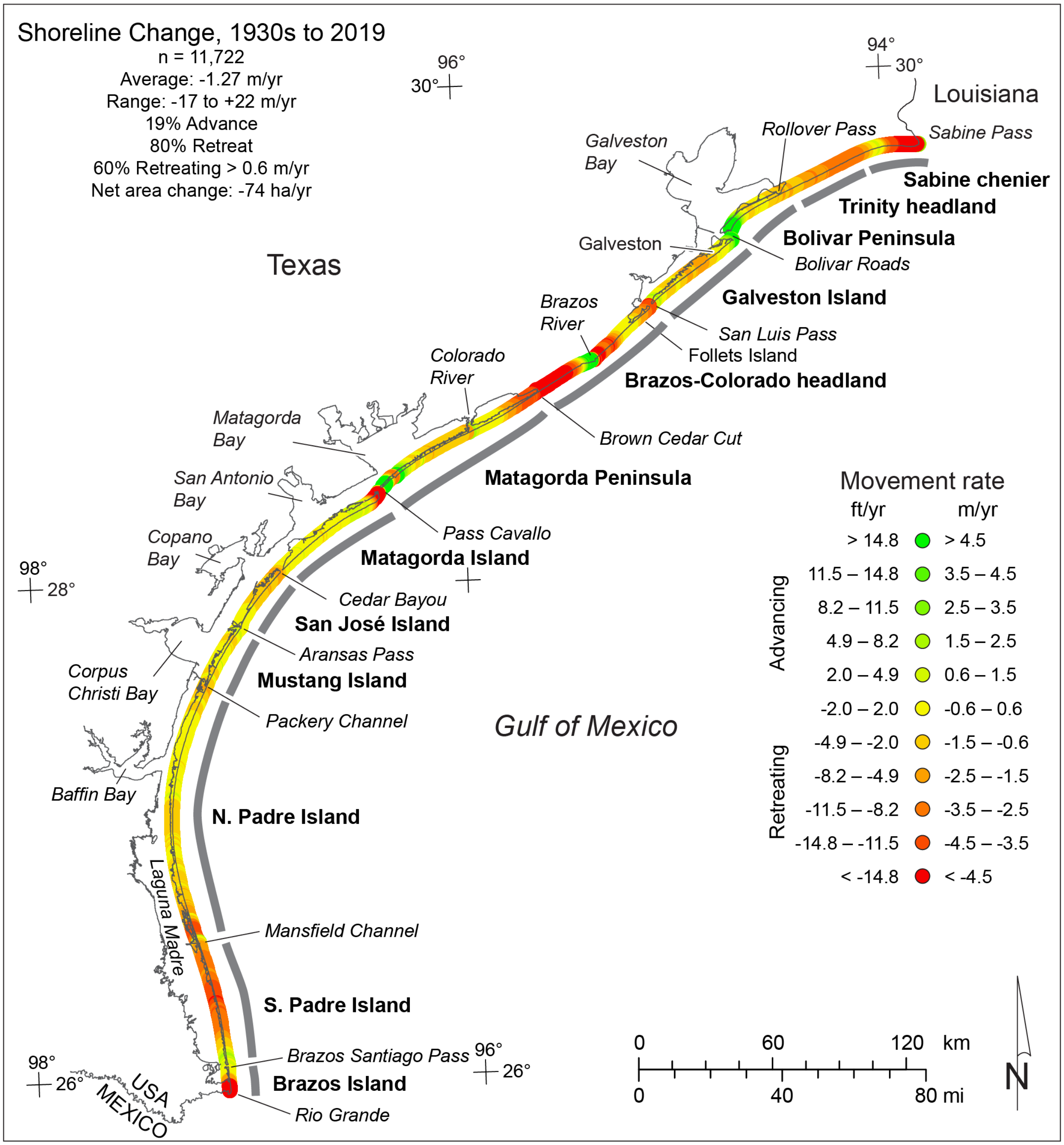


Figure 14. Net rates of long-term movement for the Texas Gulf shoreline between Sabine Pass and the Rio Grande calculated from shoreline positions from the 1930s to 2019.

Table 4. Net shoreline and land-area change between the 1930s and 2019 for the Texas Gulf shoreline and major geomorphic areas (fig. 14) with shoreline on the Gulf of Mexico.

| Area | No. | Net rate (m/yr) | Std. dev. (m/yr) | Range (m/yr) | Area change rate (ha/yr) | Area change (ha) |
|---|---|---|---|---|---|---|
| All Texas sites | 11,722 | -1.27 | 2.77 | -16.5 to +22.0 | -74.5 | -6,627 |
| | | | | | | |
| **Geomorphic Areas** | | | | | | |
| Sabine Pass to Rollover Pass | 1,345 | -3.03 | 2.64 | -11.6 to +10.6 | -20.4 | -1,814 |
| Bolivar Peninsula | 542 | +0.28 | 2.60 | -1.9 to +14.2 | +0.75 | +67 |
| Galveston Island (all) | 932 | -0.21 | 1.76 | -2.5 to +5.9 | -0.98 | -87 |
| Galv. Is. (no seawall) | 704 | -0.22 | 1.99 | -2.5 to +5.9 | -0.78 | -70 |
| Galv. Is. (East Beach) | 108 | +3.66 | 1.38 | +1.6 to +5.9 | +2.0 | +176 |
| Galv. Is. (West Beach) | 596 | -0.93 | 1.06 | -2.5 to +3.8 | -2.8 | -246 |
| Brazos–Colorado headland | 1,244 | -2.16 | 4.79 | -13.2 to +18.1 | -13.4 | -1,194 |
| Matagorda Peninsula | 1,589 | -0.89 | 2.84 | -12.2 to +22.0 | -7.1 | -631 |
| Matagorda Island | 1,116 | -0.91 | 3.70 | -16.5 to +14.4 | -5.1 | -452 |
| San José Island | 622 | -0.84 | 0.67 | -1.9 to +0.8 | -2.6 | -231 |
| Mustang Island | 574 | -0.29 | 0.52 | -1.4 to +1.7 | -0.83 | -74 |
| N. Padre Island | 2,403 | -0.77 | 0.93 | -4.4 to +1.0 | -9.2 | -820 |
| S. Padre Island | 1,120 | -2.46 | 1.51 | -4.7 to +2.8 | -13.8 | -1,227 |
| Brazos Island | 235 | -1.57 | 2.60 | -7.2 to +2.3 | -1.8 | -164 |

2019, is 74 ha/yr (184 ac/yr). Total Texas Gulf shoreline land loss from 1930 through 2019 is estimated to be 6,627 ha (16,375 ac).

### Recent Gulf Shoreline Movement, 2000 to 2019

One approach to assess whether shoreline movement rates are increasing, decreasing, or remaining constant over time is to compare long-term rates with rates measured over shorter and more recent periods. Coast-wide data on shoreline position are available from aerial imagery acquired since the 1930s, GPS surveys in the 1990s, and from airborne lidar surveys conducted in 2000, 2012, and 2019. We have augmented the long-term rates (1930s to 2019, fig. 14; table 4) with additional analyses for 2000 to 2019, the most recent period for which we have comparable lidar data coverage (fig. 15; table 5).

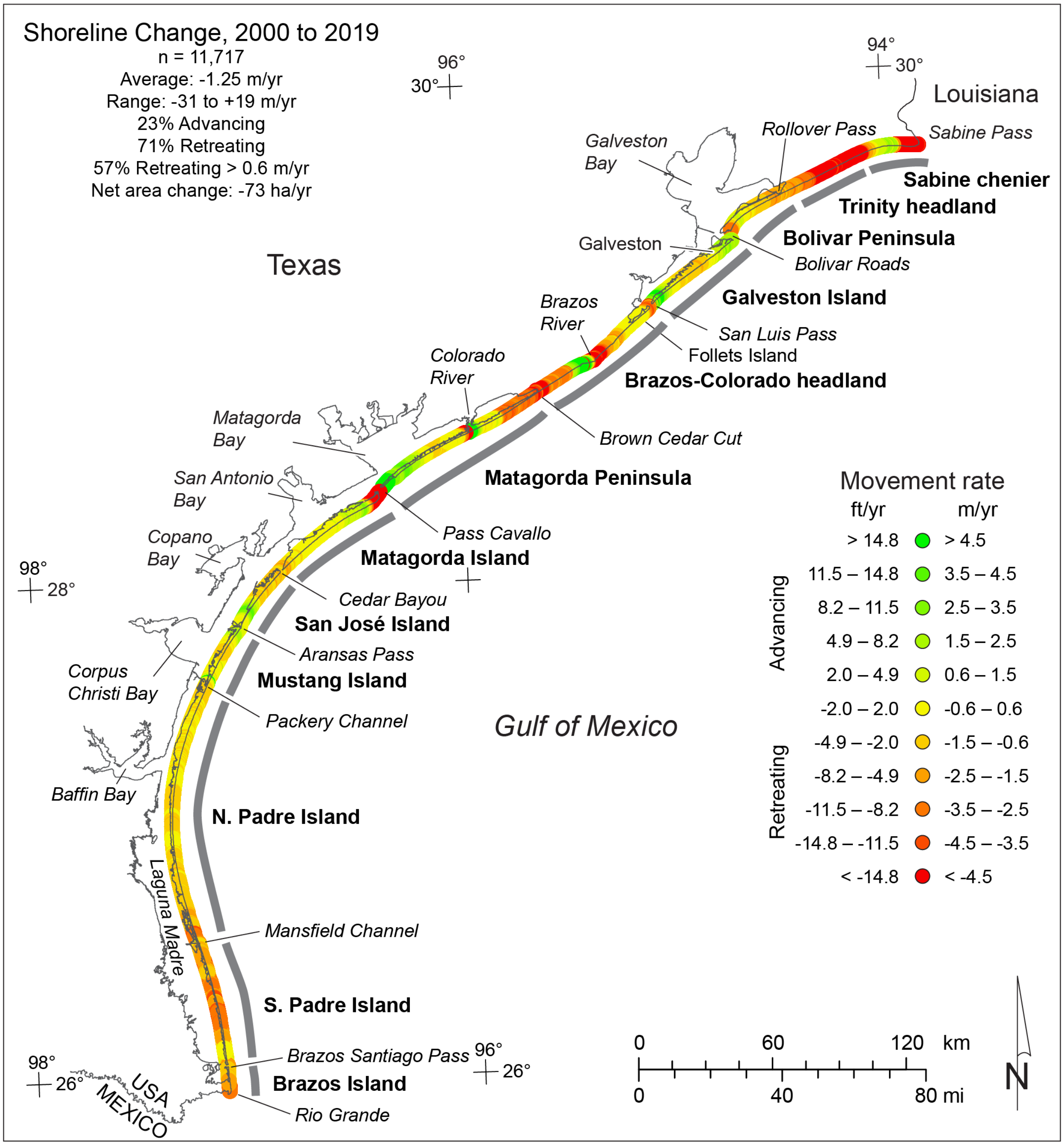


Figure 15. Net rates of recent, short-term movement for the Texas Gulf shoreline between Sabine Pass and the Rio Grande calculated from shoreline positions from 2000 to 2019.

Table 5. Net shoreline and land-area change between 2000 and 2019 for the entire Texas Gulf shoreline and major geomorphic areas (fig. 15) with shoreline on the Gulf of Mexico.

| **Area** | **No.** | **Net rate (m/yr)** | **Std. dev. (m/yr)** | **Range (m/yr)** | **Area change rate (ha/yr)** | **Area change (ha)** |
|---|---|---|---|---|---|---|
| All Texas sites | 11,717 | -1.25 | 3.25 | -30.6 to +18.5 | -73.1 | -1,389 |
| | | | | | | |
| **Geomorphic Areas** | | | | | | |
| Sabine Pass to Rollover Pass | 1,345 | -4.49 | 3.63 | -12.7 to +2.9 | -30.2 | -573 |
| Bolivar Peninsula | 542 | -0.88 | 0.99 | -2.8 to +1.5 | -2.4 | -45 |
| Galveston Island (all) | 930 | +0.77 | 1.91 | -2.0 to +11.0 | +3.6 | +68 |
| Galv. Is. (no seawall) | 704 | +0.68 | 2.11 | -2.0 to +11.0 | +2.4 | +46 |
| Galv. Is. (East Beach) | 108 | +1.94 | 0.51 | +0.2 to +3.3 | +1.0 | +20 |
| Galv. Is. (West Beach) | 596 | +0.45 | 2.21 | -2.0 to +11.0 | +1.4 | +26 |
| Brazos–Colorado headland | 1,244 | -1.66 | 4.36 | -30.6 to +9.2 | -10.3 | -196 |
| Matagorda Peninsula | 1,586 | -0.20 | 3.87 | -14.2 to +18.5 | -1.6 | -31 |
| Matagorda Island | 1,116 | -1.65 | 4.83 | -24.1 to +3.4 | -9.2 | -175 |
| San José Island | 622 | -0.07 | 1.65 | -2.4 to +4.8 | -0.21 | -4 |
| Mustang Island | 574 | +0.15 | 0.97 | -1.2 to +5.4 | +0.42 | +8 |
| N. Padre Island | 2,403 | -0.82 | 0.76 | -4.0 to +7.1 | -9.8 | -187 |
| S. Padre Island | 1,120 | -1.99 | 1.26 | -5.0 to +1.3 | -11.2 | -212 |
| Brazos Island | 235 | -1.91 | 0.88 | -4.1 to +0.7 | -2.2 | -43 |

Overall, change patterns are similar for the shorter monitoring period (figs. 14 and 15). Major areas of shoreline retreat and advance are similar, but average rates of change differ among the periods for the entire coast as well as for major geomorphic features (fig. 16), and there is a higher percentage of shoreline that advanced during the most recent monitoring period. Average retreat rate for the entire coast is slightly higher over the long-term (1930s to 2019) monitoring period (retreat at 1.27 m/yr [4.2 ft/yr]) than it is over the most recent, short-term (2000 to 2019) monitoring period (retreat at 1.25 m/yr [4.1 ft/yr]). Percentages of sites advancing or retreating show a similar pattern: the shoreline retreated at a greater proportion of sites between the 1930s and 2019 (80 percent) than it did during the most recent monitoring period between 2000 and

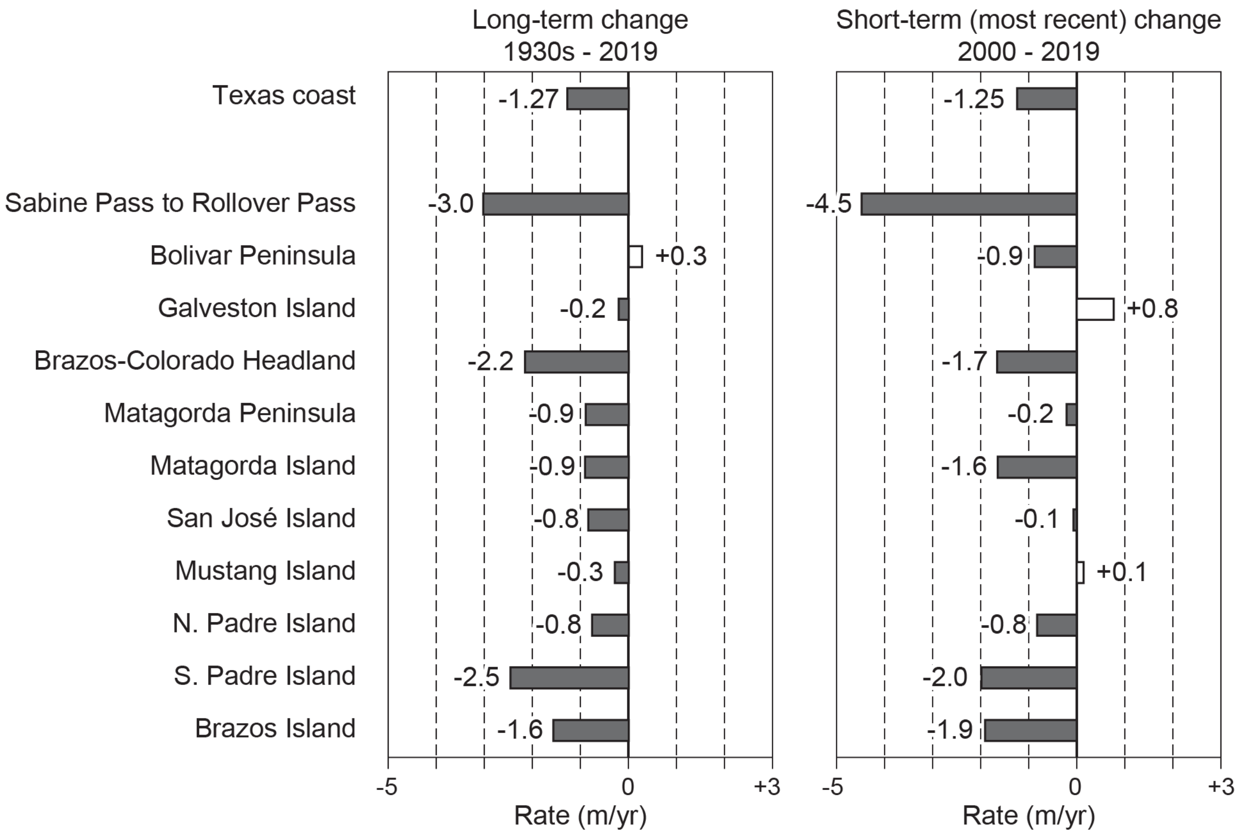


Figure 16. Comparison of long-term and most recent short-term net rates of shoreline movement for the Texas Gulf shoreline between Sabine Pass and the Rio Grande calculated from shoreline positions between the 1930s and 2019 and 2000 and 2019. Also shown are net rates for major geomorphic units along the coast.

2019 (71 percent). Estimated land-loss rates for the most recent period are 73 ha/yr (181 ac/yr), nearly identical to long-term land-loss rates of 74 ha/yr (184 ac/yr).

### Upper Texas Coast (Sabine Pass to San Luis Pass)

The upper Texas coast extends from Sabine Pass at the Texas–Louisiana border to San Luis Pass at the southwestern end of Galveston Island (figs. 14 and 17), a distance of about 141 km (88 mi). Major natural geomorphic features (fig. 14) and shoreline types are (1) the Sabine chenier, composed of generally shore-parallel beach ridges and intervening swales in the Sabine Pass area, (2) the Trinity headland, where thin, discontinuous sandy beaches and washover deposits rest on retreating low, muddy marsh deposits between Sea Rim State Park and High

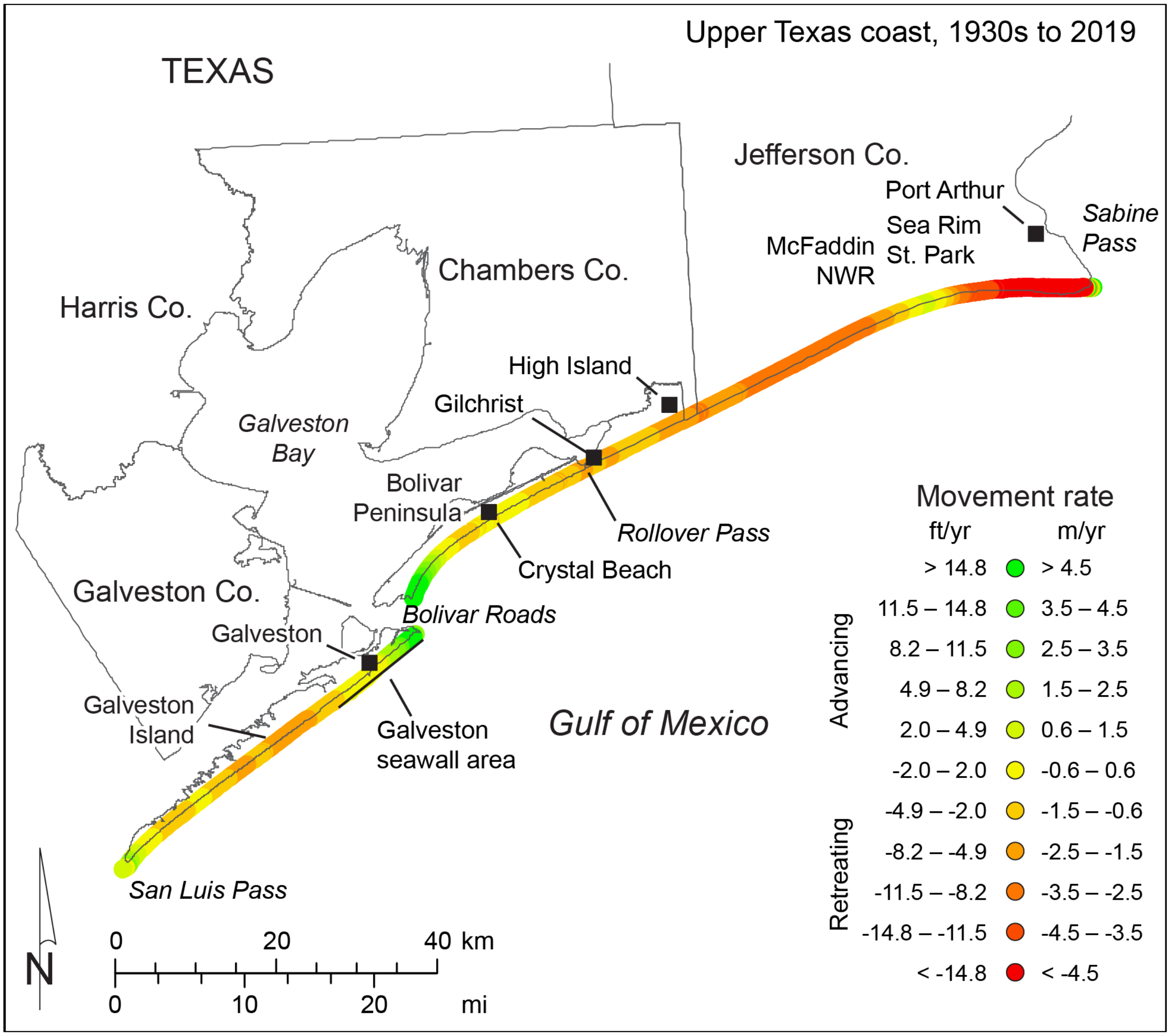


Figure 17. Net rates of long-term movement for the upper Texas Gulf shoreline between Sabine Pass and San Luis Pass (Sabine chenier, Trinity headland, and Galveston Island, fig. 14) calculated from shoreline positions between the 1930s and 2019 (table 3).

Island, (3) the broad, sandy beach and dune system on Bolivar Peninsula, and (4) the sandy barrier-island system at Galveston Island. Net longshore drift directions are eastward from the Trinity headland toward Sabine Pass, westward from the headland to Bolivar Roads, and eastward along Galveston Island, although longshore drift occurs in both directions depending on wave and wind conditions. Major engineered structures that have affected the sediment budget and shoreline change rates include major jetty and dredged channel systems at Sabine Pass and

Bolivar Roads, a shallow (1.5 m [5 ft]) dredged channel across Bolivar Peninsula at Rollover Pass (scheduled for closure in 2020), and the seawall and groin system on the eastern part of Galveston Island. Sand has also been added to the system artificially through periodic and site-specific beach nourishment projects. At Sabine Pass, the south jetty extends about 4 km (2.5 mi) from the shoreline and protects a channel maintained at a depth of 12 m (40 ft). The Sabine Pass jetties and channel isolate the upper Texas coast from potential easterly sources of longshore sediment. The Bolivar Roads channel, maintained at a depth of 14 m (45 ft), is protected by jetties that extend 7.6 km (4.7 mi) (north jetty) and 3.9 km (2.4 mi) (south jetty) from the shoreline. The jetties and channel compartmentalize the upper Texas coast by blocking longshore transport of sand between Bolivar Peninsula and Galveston Island.

About 81 percent of the measurement sites on the upper Texas coast (2,273 of 2,819) showed net shoreline retreat from the 1930s through 2019. Net rates at individual measuring points on the upper Texas coast range from retreat at 11.6 m/yr (38 ft/yr) to advance at 14.2 m/yr (47 ft/yr). Net land loss since 1930 is estimated to be 1,814 ha (4,482 ac) between Sabine Pass and Rollover Pass and 87 ha (215 ac) on Galveston Island (table 4). There was a net land gain of 67 ha (166 ac) on Bolivar Peninsula west of Rollover Pass. Long segments of retreating shorelines extend from near Sabine Pass to High Island, along Bolivar Peninsula near Gilchrist and southwest of Crystal Beach, and on Galveston Island from the west end of the seawall to near San Luis Pass (fig. 17). Areas of net advance are limited, but include a 3-km (2-mi)-long segment at Sea Rim State Park and McFaddin National Wildlife Refuge, a short shoreline segment adjacent to the south jetty at Sabine Pass, shoreline segments extending 7.3 km (4.5 mi) north and 12 km (7.5 mi) south of the jetties at Bolivar Roads, and the southwestern end of Galveston Island extending about 4.3 km (2.7 mi) from San Luis Pass.

The shoreline between Sabine Pass and Rollover Pass has the highest rate of net shoreline retreat (3.03 m/yr [9.9 ft/yr]) observed on the Texas coast between the 1930s and 2019 (table 4). Conversely, Bolivar Peninsula and Galveston Island have among the lowest net rates of shoreline movement since the 1930s: there is net shoreline advance at 0.28 m/yr (0.9 ft/yr) on Bolivar Peninsula, whereas Galveston Island shorelines retreated at a low net rate of 0.21 m/yr (0.7 ft/yr). In these areas, shoreline advance adjacent to the Bolivar Roads jetties offsets shoreline retreat farther from the jetties. On Galveston Island, for example, the East Beach area adjacent to the jetty advanced at a net rate of 3.66 m/yr (12.0 ft/yr) between the 1930s and 2019, whereas Galveston Island shorelines west of the seawall retreated at average net rates of 0.93 m/yr (3.0 ft/yr) during the same period.

Comparisons of long-term (1930s to 2019) rates on the upper Texas coast (fig. 17; table 4) with those calculated for the most recent period (2000 to 2019) (fig. 18; table 5) show similar patterns of shoreline movement. Since 2000, most of the shoreline northeast of Rollover Pass has retreated, with the exception of the Sea Rim State Park area, where the shoreline underwent net advance during the most recent monitoring period. Relatively high and accelerating rates of retreat on the upper coast between Sabine Pass and Rollover Pass (average rates of retreat at 4.49 m/yr [14.7 ft/yr] along this segment between 2000 and 2019) are the highest for the period on the entire coast (fig. 16). Bolivar Peninsula, the only major geomorphic feature showing long-term net advance, underwent net retreat at 0.88 m/yr (2.9 ft/yr) during the 2000 to 2019 period (fig. 16). For Galveston Island as a whole, minimal average net retreat rates between the 1930s and 2019 contrast with average short-term net rates of advance of 0.77 m/yr (2.5 ft/yr) between 2000 and 2019. The eastern and western ends of Galveston Island underwent net shoreline advance between 2000 and 2019, while the central part of the island west of the seawall was stable to erosional.

### Brazos and Colorado Headland and Adjacent Peninsulas (San Luis Pass to Pass Cavallo)

Between San Luis Pass and Pass Cavallo lie the headland of the Brazos and Colorado river deltas and adjacent barrier peninsulas: Follets Island and Matagorda Peninsula (figs. 14 and 19). This segment includes about 143 km (89 mi) of Gulf of Mexico shoreline. Major geologic features are (1) Follets Island, a narrow, sandy barrier peninsula extending northeastward from the Brazos

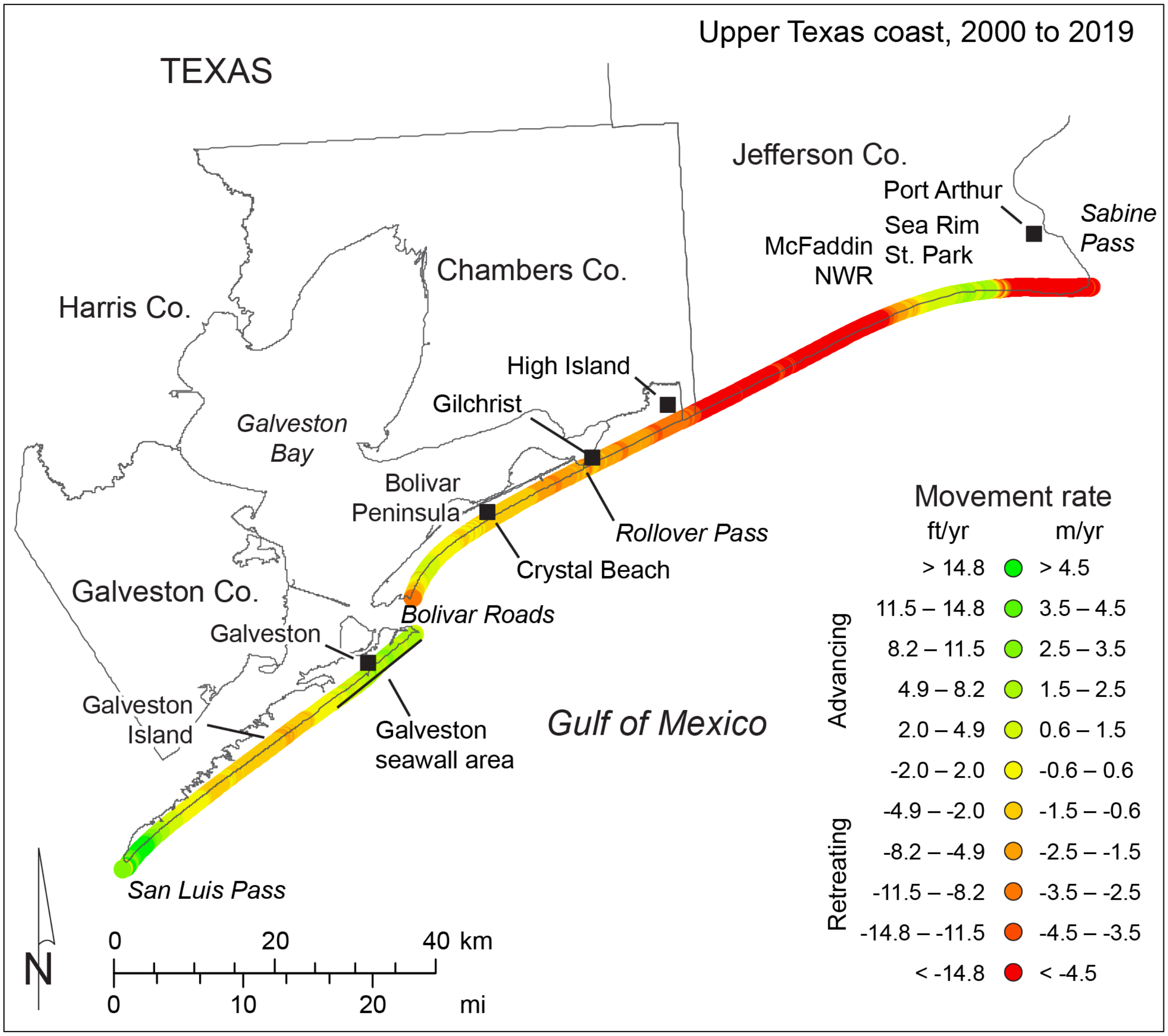


Figure 18. Net rates of recent, short-term movement for the upper Texas Gulf shoreline between Sabine Pass and San Luis Pass (Sabine chenier, Trinity headland, and Galveston Island, fig. 15) calculated from shoreline positions between 2000 and 2019 (table 3).

headland toward San Luis Pass; (2) the Brazos and Colorado deltaic headland, consisting of semiconsolidated, muddy and sandy sediments deposited by the Brazos and Colorado rivers and overlain by a discontinuous, thin veneer of sandy beach deposits; and (3) Matagorda Peninsula, a narrow, sandy barrier peninsula extending southwestward from the Colorado headland from Sargent Beach to Pass Cavallo. Sediments eroded by waves at the headland contribute sand to the flanking barrier peninsulas. In addition, the Brazos and Colorado rivers historically brought

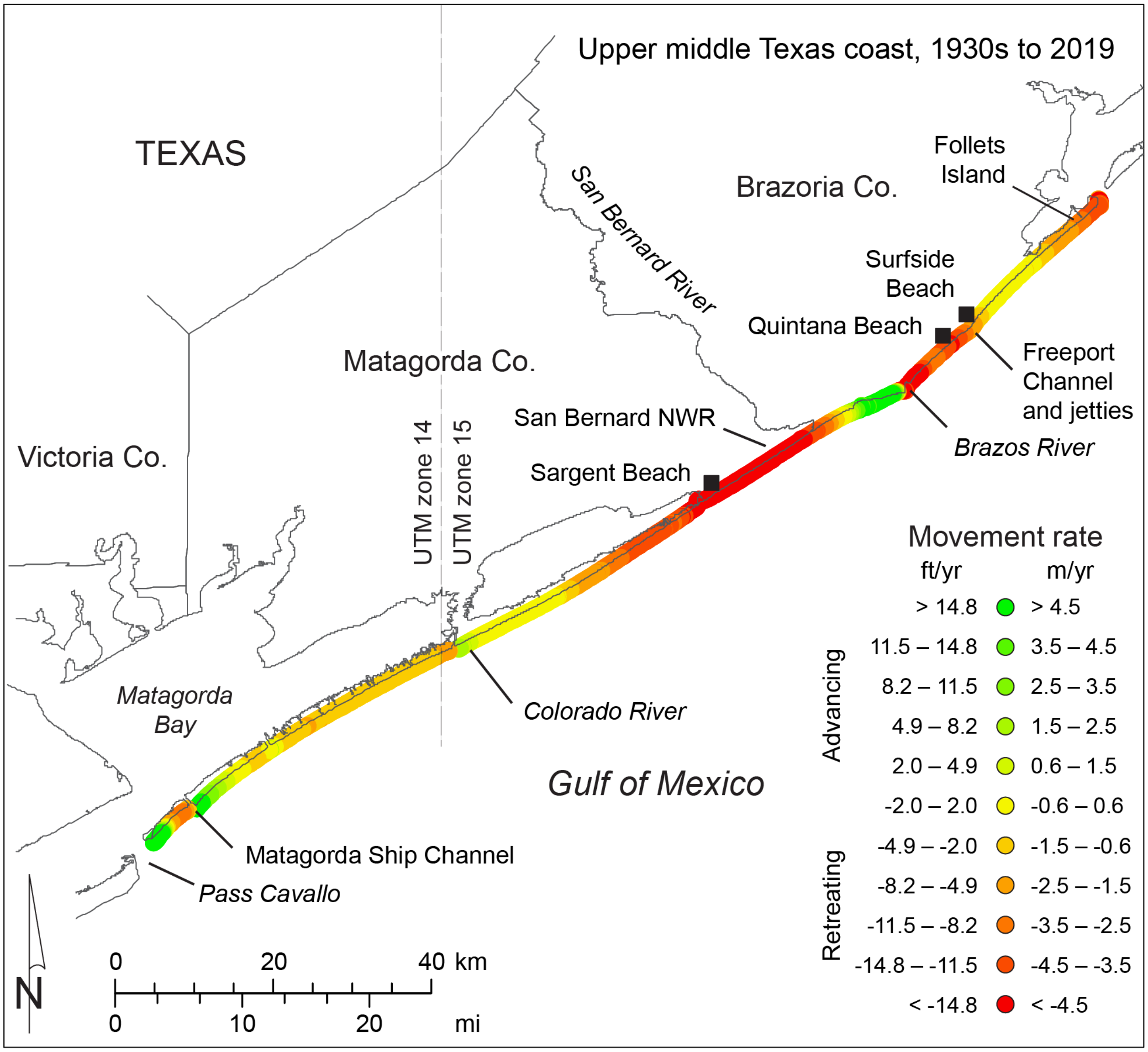


Figure 19. Net rates of long-term movement for the Texas Gulf shoreline between San Luis Pass and Pass Cavallo (Brazos and Colorado headland, Follets Island, and Matagorda Peninsula; fig. 14) calculated from shoreline positions between the 1930s and 2019 (table 3).

sediment to the coast from their large drainage basins. The drainage basin of the Brazos River covers more than 116,000 km$^2$ (45,300 mi$^2$) in Texas and eastern New Mexico, but its capacity for carrying sediment to the coast during major floods has been reduced by completion of several dams and reservoirs between 1941 and 1969 (Possum Kingdom, Whitney, Granbury, and DeCordova Bend). The drainage basin of the Colorado is nearly as large (103,000 km$^2$) [41,600 mi$^2$], but its sediment load has also been reduced by nine dams completed in the upper and central basins between 1937 and 1990 (Buchanan, Inks, Tom Miller, Mansfield, Wirtz, Starcke, Thomas, Lee, and Ivie), reductions in flood frequency and flow, and diversion into Matagorda Bay. This segment of Gulf shoreline has been compartmentalized by jetties and dredged channels. Between Quintana Beach and Surfside Beach, the Freeport jetties extend about 1,000 m (3,300 ft) from the shoreline to reduce dredging needs of the Freeport Ship Channel, which has been dredged to a depth of 14 m (45 ft). On Matagorda Peninsula, shorter jetties extend 140 to 240 m (460 to 790 ft) seaward from the mouth of the Colorado River. The Matagorda Ship Channel, maintained at a depth of 11 m (36 ft) near the southwestern end of Matagorda Peninsula, is flanked by jetties that extend 880 m (2,900 ft) (north jetty) and 1,600 m (5,250 ft) (south jetty) into the Gulf.

There was net shoreline retreat at 2,327 of 2,833 measurement sites (82 percent) between San Luis Pass and Pass Cavallo between the 1930s and 2019 (fig. 19). Net rates of change through 2019 ranged from retreat at 13.1 m/yr (43.2 ft/yr) to advance at 22.0 m/yr (72.0 ft/yr). Notable areas of long-term shoreline retreat include Follets Island, the Brazos–Colorado headland between Surfside Beach and the mouth of the Brazos River and from the mouth of the San Bernard River to Sargent Beach (including the frontage of the San Bernard Wildlife Refuge), Matagorda Peninsula southwest of Sargent Beach, and Matagorda Peninsula southwest of the Matagorda Ship Channel (fig. 19). Shorelines having net long-term advance include a 3.2-km (2.0 mi)-long segment on the Brazos–Colorado headland northeast of Surfside Beach, a 7.7-km (4.8-mi)-long segment southwest of the mouth of the Brazos River, and short segments on Matagorda Peninsula that include a 2.5-km (1.6-mi) long segment northeast of the mouth of the Colorado River, a 6.3-km (3.9-mi)-long segment adjacent to the north jetty at the Matagorda Ship Channel, and a 2.4-km (1.5-mi)-long segment at the southwestern tip of Matagorda Peninsula.

Average net movement on the Brazos–Colorado headland (including Follets Island) between the 1930s and 2019 was retreat at 2.16 m/yr (7.1 ft/yr) (fig. 16; table 4), translating to a net land-loss rate of 13.4 ha/yr (33.1 ac/yr). Total land loss on the headland since 1930 is estimated to be 1,194 ha (2,950 ac) (table 4). Average long-term retreat rates are 0.89 m/yr (2.9 ft/yr) on Matagorda Peninsula. Land-loss rates on Matagorda Peninsula are estimated at 7.1 ha/yr (17.5 ac/yr) between the 1930s and 2019. Total land loss on Matagorda Peninsula between 1930 and 2019 is estimated to be 631 ha (1,558 ac).

During the most recent short-term monitoring period between 2000 and 2019, shoreline movement patterns are similar to those of the long-term period, but rates are generally less recessional (figs. 19 and 20). Average net rates of retreat on the Brazos–Colorado headland decreased to 1.66 m/yr (5.5 ft/yr) (fig. 16; table 5). On Matagorda Peninsula, there was net shoreline retreat at 0.20 m/yr (0.7 ft/yr) between 2000 and 2019. Advancing shoreline segments were more extensive in the most recent period; significant shoreline advance was measured along much of Follets Island (except near San Luis Pass), between the Brazos River and the San Bernard River, on Matagorda Peninsula northeast of the mouth of the Colorado River, and on the southwestern part of Matagorda Peninsula (fig. 20).

### Middle Texas Coast (Pass Cavallo to Packery Channel)

Gulf shorelines along the middle Texas coast between Pass Cavallo and Packery Channel include those on three sandy barrier islands: Matagorda Island, San José Island, and Mustang Island (figs. 15 and 21). These generally sand-rich islands are characterized by broad, sandy beaches and dune systems that reflect the position of the islands within a longshore current convergence zone between the Brazos–Colorado and Rio Grande fluvial and deltaic headlands. The natural boundaries between these three islands are Cedar Bayou, a tidal inlet between Matagorda and San José Islands, and Aransas Pass, a tidal inlet between San José and Mustang Islands. No rivers directly reach the Gulf within this segment.

Engineered structures that have compartmentalized the nearshore system are (1) the Matagorda Ship Channel and jetties that restrict sediment transport to Matagorda Island from the northeast, and (2) the jetties at Aransas Pass, which protect the dredged, 14-m (47-ft) deep Corpus Christi

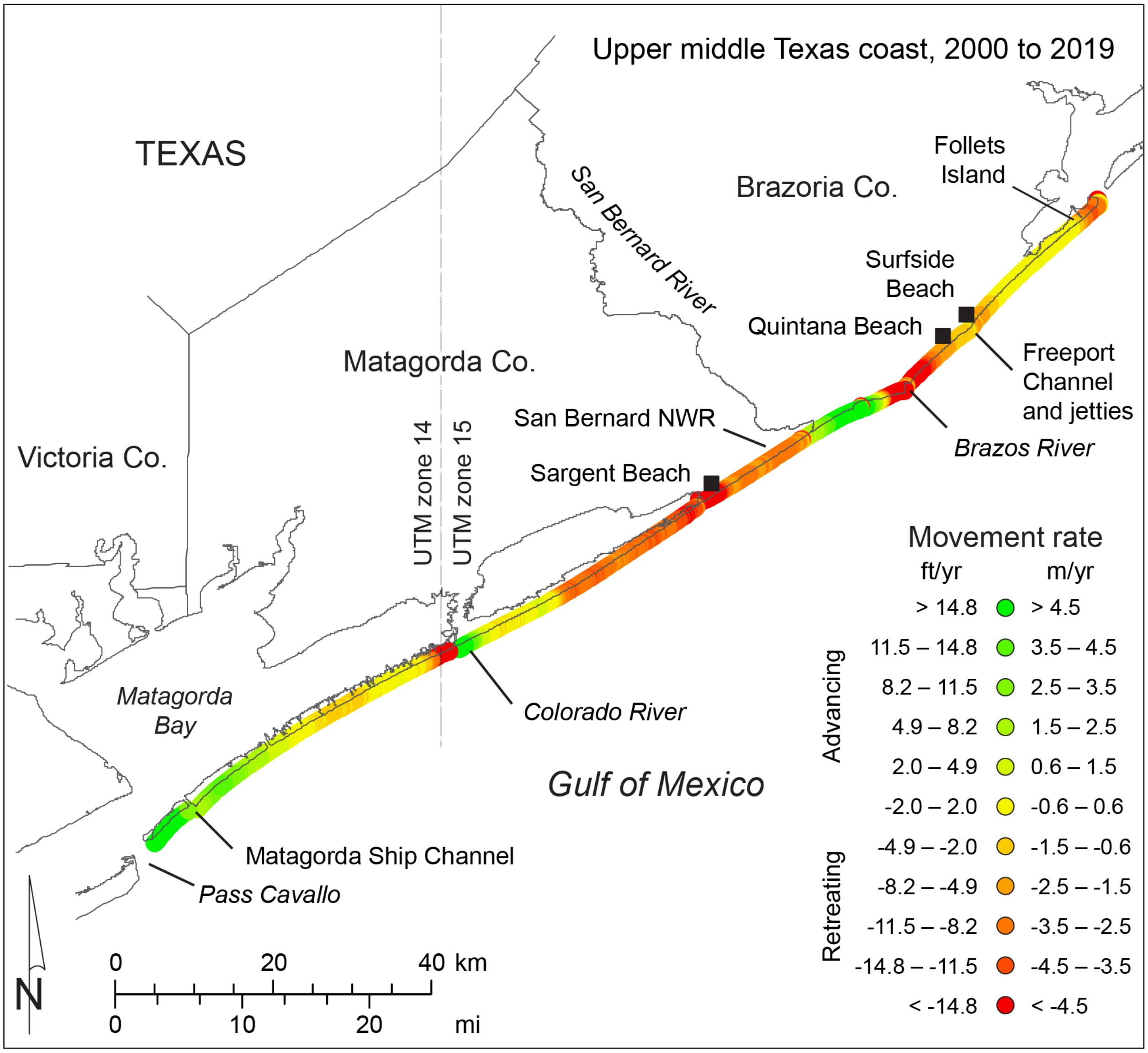


Figure 20. Net rates of recent, short-term movement for the Texas Gulf shoreline between San Luis Pass and Pass Cavallo (Brazos and Colorado headland, Follets Island, and Matagorda Peninsula; fig. 15) calculated from shoreline positions between 2000 and 2019 (table 3).

Ship Channel. Plans are underway to deepen the Corpus Christi channel to 16 m (52 ft). These jetties extend 1,100 to 1,200 m (3,600 to 3,950 ft) gulfward from the shoreline, interrupting bidirectional longshore sand exchange between Mustang Island and San José Island. Smaller structures with possible local effects include the closed Fish Pass on Mustang Island, where the former dredged channel is filled but short jetties that extend about 150 m (500 ft) from the shoreline remain; and Packery Channel, a shallow channel between Mustang Island and

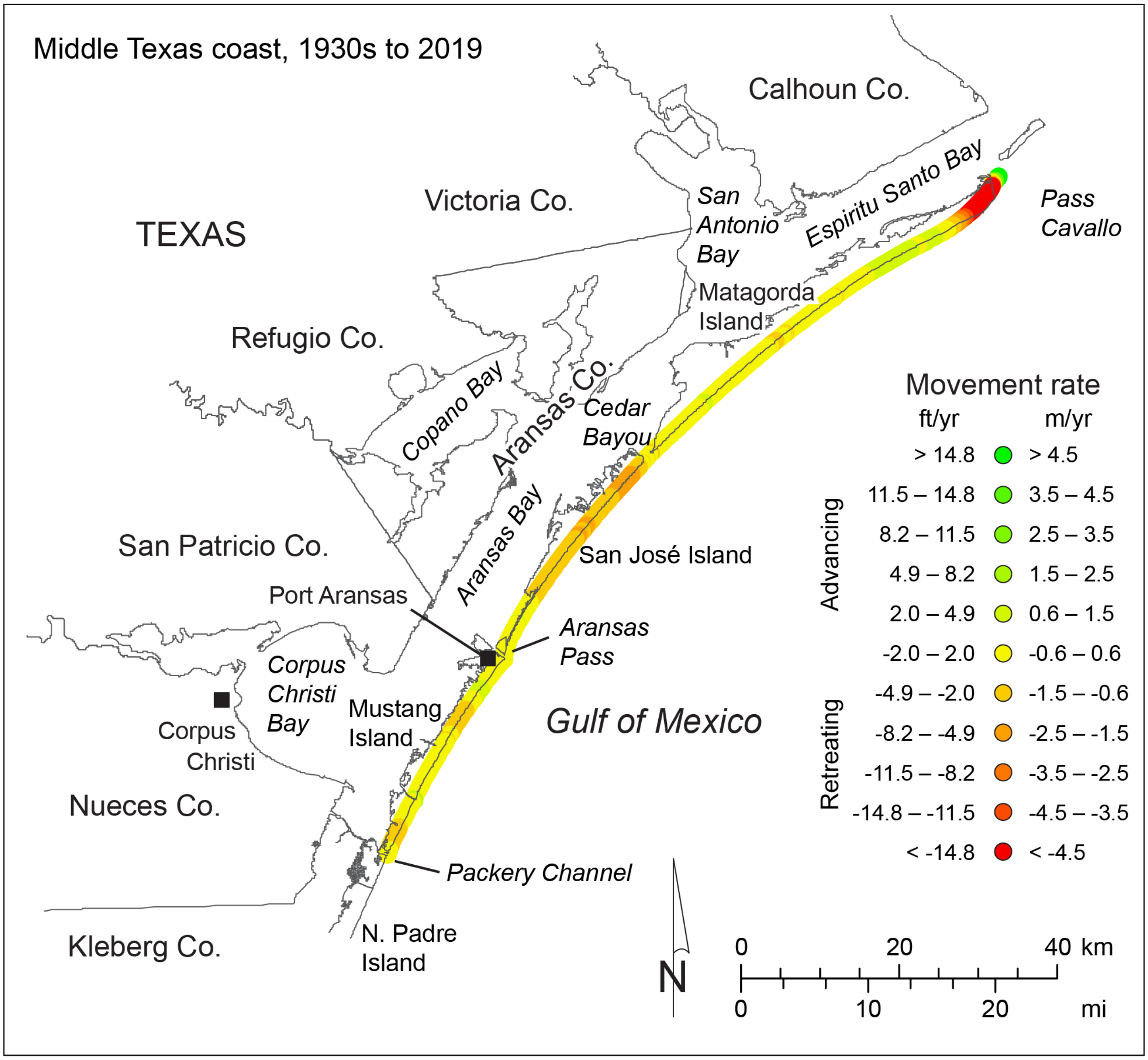


Figure 21. Net rates of long-term movement for the middle Texas Gulf shoreline between Pass Cavallo and the Packery Channel area (Matagorda Island, San José Island, and Mustang Island) calculated from shoreline positions between the 1930s and 2019 (table 3).

Padre Island that has been dredged to a nominal depth of 3 m (10 ft) and is protected by jetties that reach 300 m (1,000 ft) (north jetty) and 365 m (1,200 ft) (south jetty) seaward of the Gulf shoreline.

Long-term Gulf shoreline change rates within this segment of the Texas coast were calculated at 2,312 sites over a distance of 115 km (71 mi) between Pass Cavallo and the southern end of

Mustang Island (table 4; fig. 21). Net shoreline change rates calculated from the 1930s to 2019 averaged retreat at 0.91 m/yr (3.0 ft/yr) for Matagorda Island, retreat at 0.84 m/yr (2.8 ft/yr) for San José Island, and retreat at 0.29 m/yr (1.0 ft/yr) for Mustang Island. Annual rates of land loss estimated from these rates are 5.1 ha/yr (12.5 ac/yr) on Matagorda Island, 2.6 ha/yr (6.4 ac/yr) on San José Island, and 0.83 ha/yr (2.1 ac/yr) on Mustang Island. Estimated total land loss along the Gulf shoreline since 1930 is 452 ha (1,116 ac) on Matagorda Island, 231 ha (572 ac) on San José Island, and 74 ha (183 ac) on Mustang Island.

Two-thirds of measuring sites underwent net shoreline retreat (1,562 of 2,312; 68 percent) from 1930 to 2019. Net rates at individual sites ranged from retreat at 16.5 m/yr (54.3 ft/yr) to advance at 14.4 m/yr (47.3 ft/yr). Almost 40 percent of the Gulf shoreline along Matagorda Island has advanced since the 1930s, albeit at low rates except along a short segment where the island has migrated toward Pass Cavallo at its northeastern end (fig. 21). Sites along short shoreline segments (6.3 to 7.2 km [3.9 to 4.5 mi] long) near the north and south jetties at Aransas Pass recorded minor net shoreline advance. Highest rates of net retreat (more than 3 m/yr [10 ft/yr]) were measured along a 6.2-km (3.8-mi)-long segment of Matagorda Island near Pass Cavallo. Net retreat rates greater than 1 m/yr (3.3 ft/yr) were measured along a 17-km (10.5 mi)-long segment of San José Island southwestward from Cedar Bayou and along a 2.7-km (1.7-mi)-long segment on the southern part of Mustang Island. Net retreat rates elsewhere were less than about 1 m/yr (3 ft/yr).

Net rates of retreat on Matagorda Island are higher for the more recent (2000 to 2019) monitoring period than they are for the longer-term period (figs. 16 and 22). The average long-term retreat rate of 0.91 m/yr (3.0 ft/yr) increased to 1.65 m/yr (5.4 ft/yr) from 2000 to 2019. Recent short-term trends on San José Island are less erosional; average net retreat rates of 0.84 m/yr (2.8 ft/yr) between the 1930s and 2019 changed to average net retreat rates of 0.07 m/yr (0.2 ft/yr) over the most recent period (2000 to 2019, fig. 22). On Mustang Island, low average rates of long-term net retreat at 0.29 m/yr (1.0 ft/yr) changed to slight net advance at 0.15 m/yr (0.5 ft/yr) during

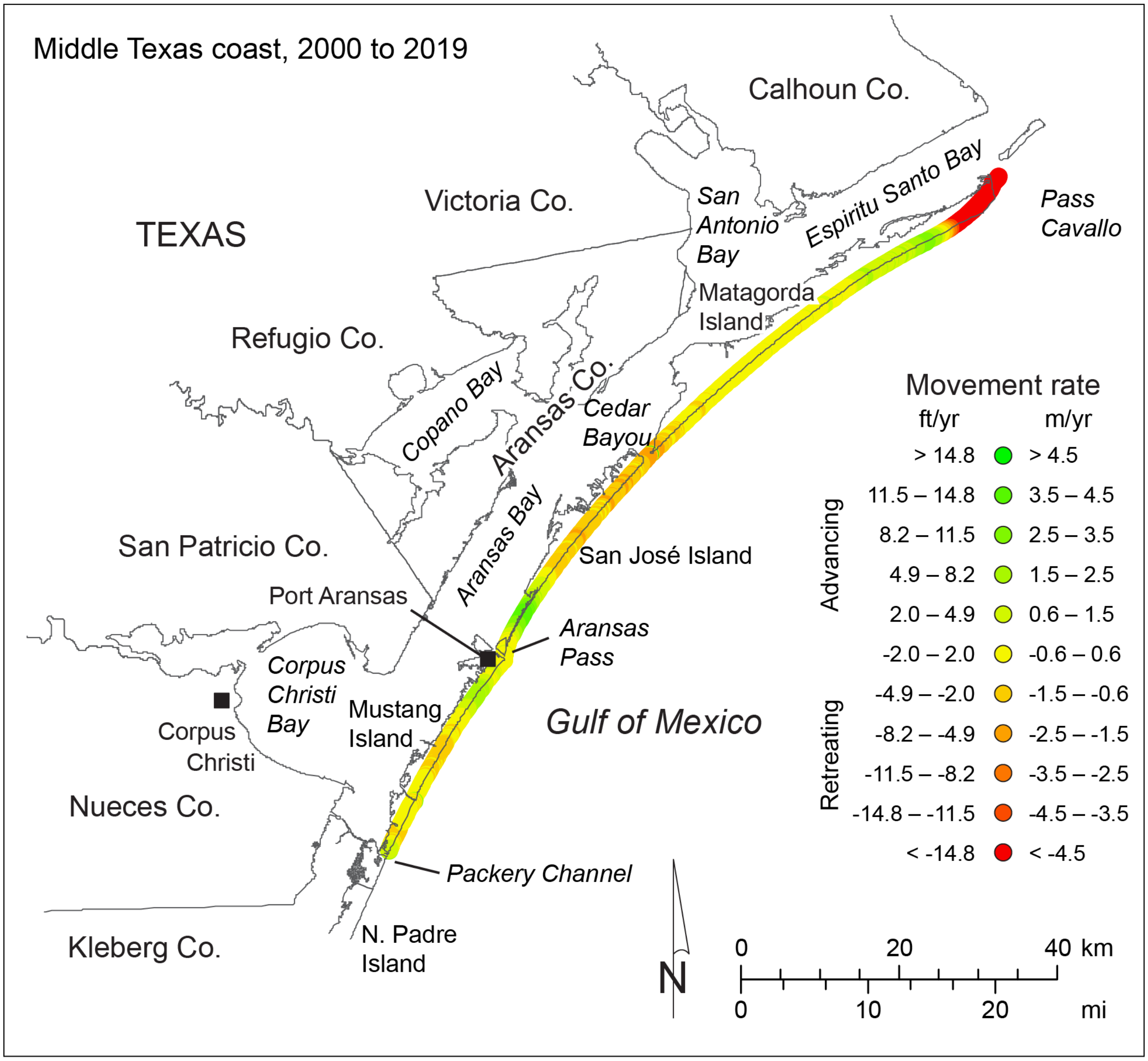


Figure 22. Net rates of recent, short-term movement for the middle Texas Gulf shoreline between Pass Cavallo and the Packery Channel area (Matagorda Island, San José Island, and Mustang Island) calculated from shoreline positions between the 2000 and 2019 (table 3).

the most recent monitoring period (2000 to 2019). Mustang Island was one of only two geologic features on the Texas coast having net shoreline advance from 2000 to 2019 (fig. 16).

### Lower Coast (Padre Island and Brazos Island)

The lower coast segment encompasses 188 km (117 mi) of Gulf shoreline between Packery Channel and the mouth of the Rio Grande (figs. 14 and 23). The principal natural geomorphic

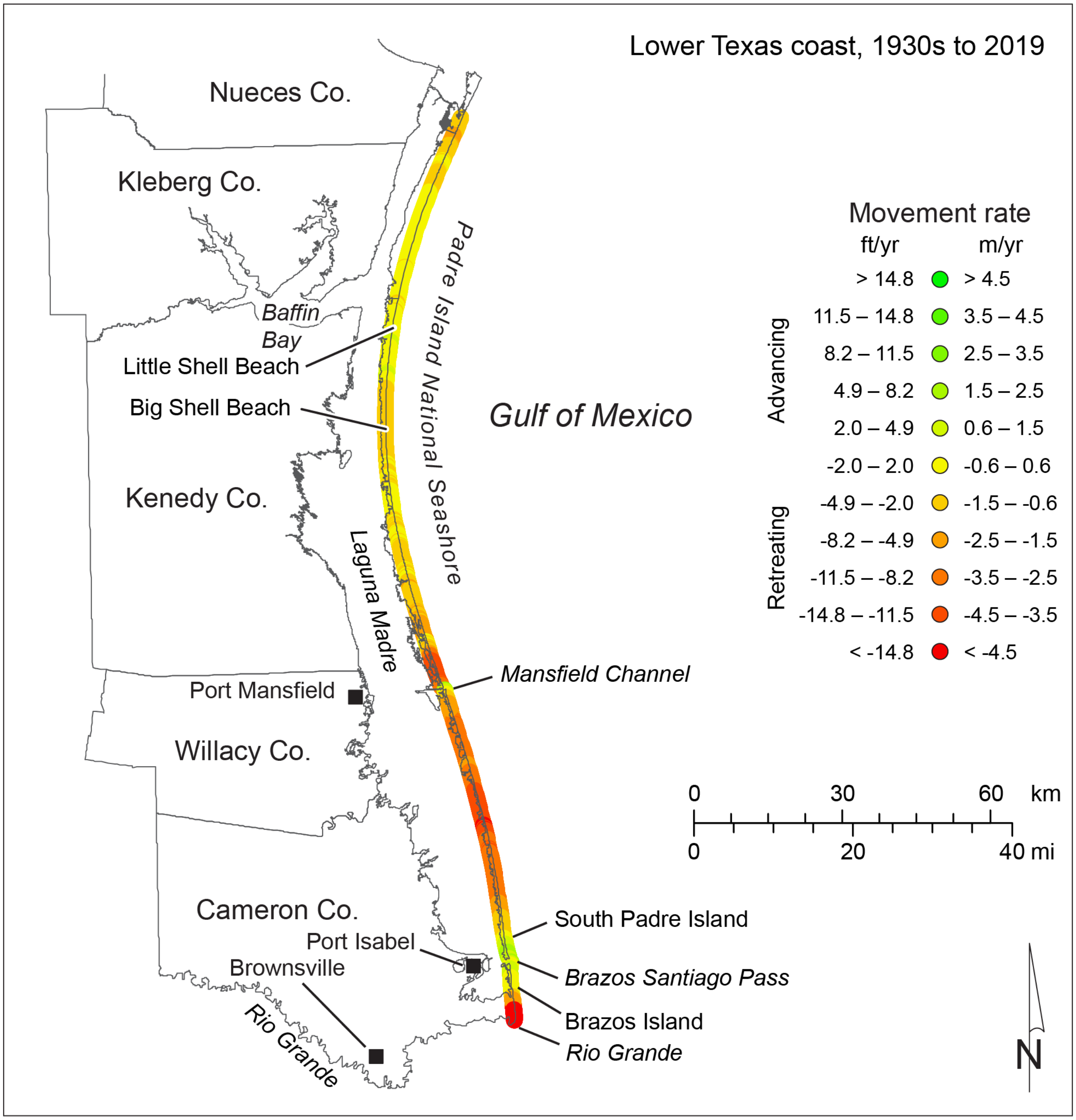


Figure 23. Net rates of long-term movement for the lower Texas Gulf shoreline between Packery Channel and the Rio Grande (Padre Island and Brazos Island) calculated from shoreline positions between the 1930s and 2019 (table 3).

feature in this area is Padre Island, a long Holocene barrier island that broadens from a narrow peninsula at Brazos Santiago Pass to a broad, sandy barrier island having a well-developed dune system throughout most of its length. Brazos Island is a short barrier island that extends southward toward the Rio Grande from Brazos Santiago Pass. The Rio Grande enters the Gulf of

Mexico at the southern end of this segment and has created a large fluvial and deltaic headland that forms the southern boundary of a regional longshore current cell that is bounded on the north by the Brazos–Colorado headland. Net longshore drift is northward on the southern part of Padre Island and southward on the northern part of the island. The Rio Grande has a large drainage basin (471,900 $km^2$ [182,200 $mi^2$]) that extends into Mexico, New Mexico, and Colorado, but dams constructed on the middle and lower parts of the basin in 1954 (Falcon) and 1969 (Amistad), combined with extensive irrigation use of Rio Grande water on the coastal plain, has reduced the sediment delivered to the coast.

Most of Padre Island is undeveloped, except for intensive development at its northern extremity and at the southern tip of the island (the city of South Padre Island). Engineering structures that have affected shoreline position include (1) the jetties and associated ship channel at Brazos Santiago Pass, where the 13-m (44-ft) deep channel is flanked by jetties that reach 870 m (2,850 ft) (north jetty) and 490 m (1,600 ft) (south jetty) into the Gulf; and (2) the shallower Port Mansfield Channel and its 620-m (2,030 ft) north jetty and 140-m (460 ft) south jetty that protect the 5-m (15-ft) deep channel. Plans are underway to deepen the ship channel to 16 m (54 ft).

Despite the favorable location of much of Padre Island in a longshore drift convergence zone, the shoreline retreated at 3,174 of 3,758 measurement sites (85 percent) between the 1930s and 2019 (fig. 23). Net change rates ranged from retreat at 7.2 m/yr (23.6 ft/yr) to advance at 2.8 m/yr (9.1 ft/yr). Average long-term net shoreline movement rates are retreat at 0.77 m/yr (2.5 ft/yr) on northern Padre Island (Mansfield Channel to Packery Channel), 2.46 m/yr (8.1 ft/yr) on southern Padre Island (Mansfield Channel to Brazos Santiago Pass), and 1.57 m/yr (5.2 ft/yr) on Brazos Island (fig. 23, table 4). Estimated net land loss since 1930 is 820 ha (2,026 ac) along northern Padre Island, 1,227 ha (3,032 ac) along southern Padre Island, and 163 ha (405 ac) along Brazos Island.

Net advancing shorelines include a 13.3-km (8.3-mi)-long segment in the Little Shell Beach area on Padre Island National Seashore near Baffin Bay, a 1-km (0.6-mi)-long segment adjacent to the south jetty at Mansfield Channel, and two nearly 5-km (3-mi)-long segments adjacent to the north and south jetties at Brazos Santiago Pass (fig. 23). Highest rates of net retreat (greater than 3 m/yr [10 ft/yr]) were measured along a 7-km (4-mi)-long segment north of the Mansfield Channel jetties, a 22-km (13.7-mi)-long segment on southern Padre Island, and a 2.8-km (1.7-mi)-long segment near the Rio Grande (fig. 23).

During the most recent, short-term monitoring period (2000 to 2019), net shoreline movement on the lower Texas coast was similar to the long-term average (figs. 16, 23, and 24). Northern Padre Island, the segment on the lower coast with the lowest long-term average retreat rate at 0.77 m/yr (2.5 ft/yr), underwent slightly higher net retreat at 0.82 m/yr (2.7 ft/yr) between 2000 and 2019 (fig. 16; table 5). Net average retreat rates for the most recent period are 1.99 m/yr (6.5 ft/yr) for southern Padre Island, lower than the long-term average of 2.46 m/yr (8.1 ft/yr). On Brazos Island, retreat rates for the 2000 to 2019 period are 1.91 m/yr (6.3 ft/yr), higher than the long-term rate of 1.57 m/yr (5.2 ft/yr) for Brazos Island (fig. 16; table 5).

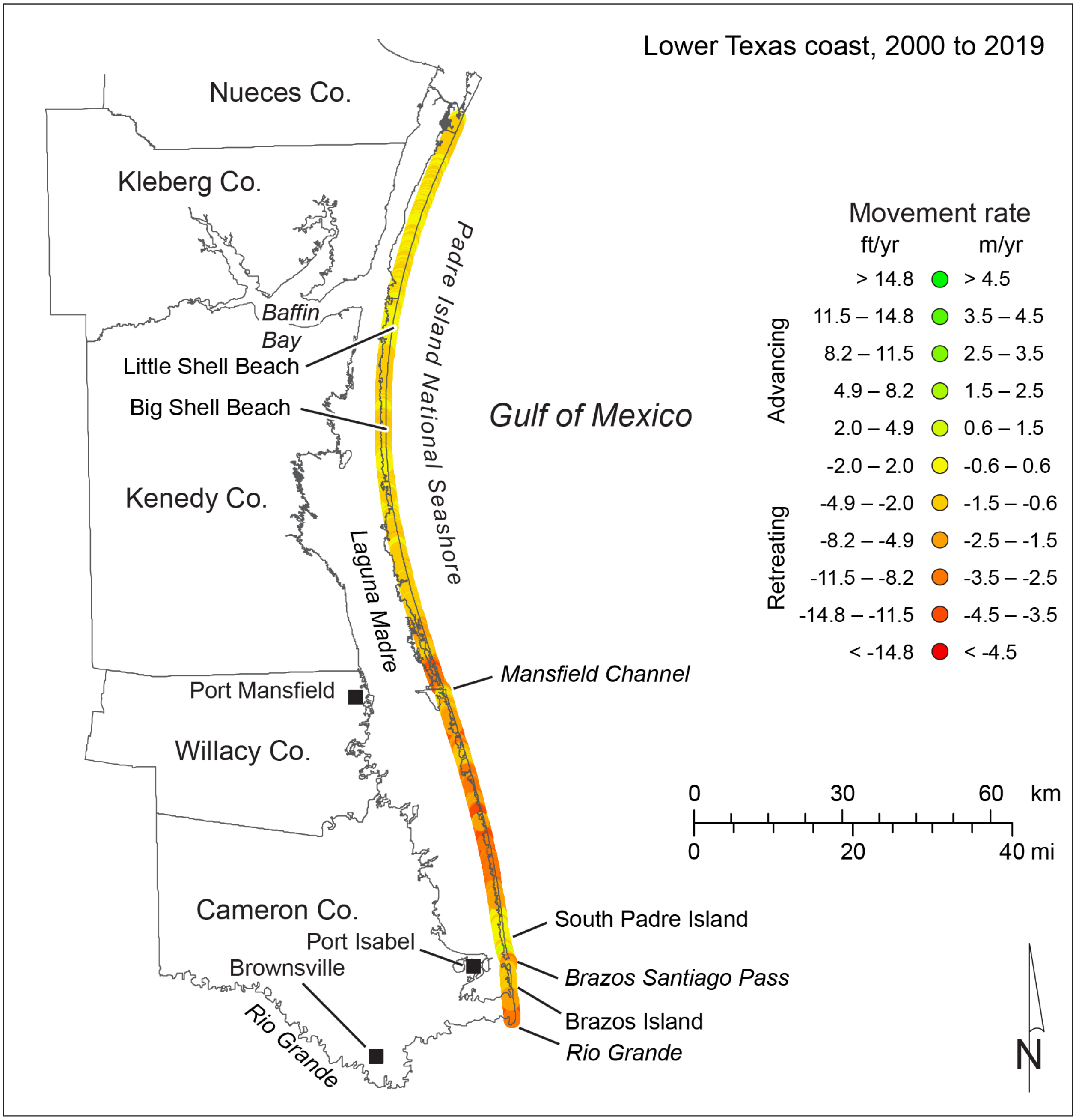


Figure 24. Net rates of recent, short-term movement for the lower Texas Gulf shoreline between Packery Channel and the Rio Grande (Padre Island and Brazos Island) calculated from shoreline positions between 2000 and 2019 (table 3).

## LATE PLEISTOCENE TO HOLOCENE CONTEXT

Estimates of shoreline-change rates over recent geologic intervals can provide a longer-term context for historical rates documented from maps, aerial photographs, beach surveys, and airborne surveys acquired over many decades. One simple approach to estimating net change rates since the end of the last glacial maximum about 20 thousand years ago (ka), when sea level was several hundred feet lower than it is today (fig. 25), is to use shelf bathymetric contours (fig. 26) as a proxy for shoreline position at past sea-level elevations. Rates of postglacial shoreline change can be estimated by measuring the shore-normal distance between selected bathymetric contours on the Texas shelf and the present shoreline position and dividing by the

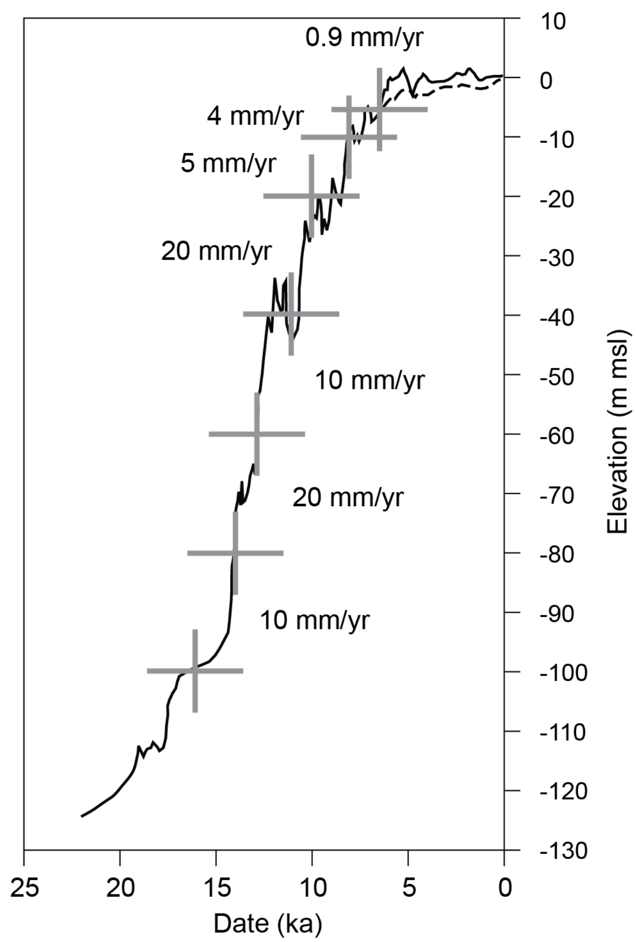


Figure 25. Postglacial Gulf of Mexico sea-level curves (Balsillie and Donoghue, 2004, 2009; Millilken and others, 2008) and approximate rates of relative sea-level rise between 16 and 14 ka, 14 and 13 ka; 13 and 11 ka; 11 and 10 ka; 10 and 8 ka, 8 and 7 ka, and 7 ka to present.

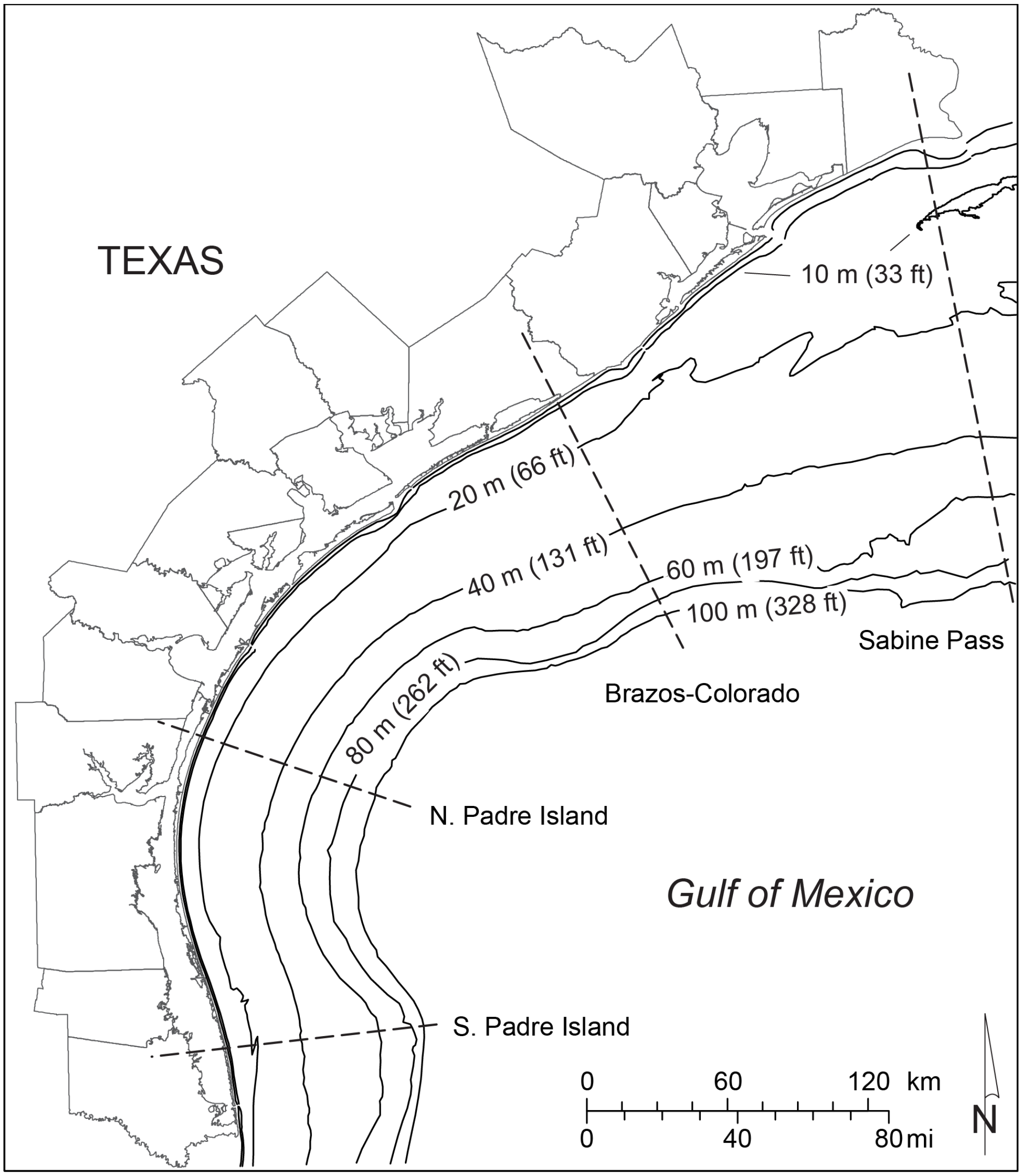

Figure 26. Major bathymetric contours on the Texas continental shelf and transect locations where postglacial net and interval shoreline migration rates are estimated using bathymetric contours as a shoreline proxy. Bathymetric data generalized from Holcombe and Arias (2009).

elapsed time since sea level was at those elevations (table 6). Subsidence, which is likely to vary spatially and temporally, is a substantial source of possible error for this approach. Nevertheless, the impact of subsidence on the rates is partly offset by the fact that the Gulf of Mexico sea-level curves (Balsillie and Donoghue, 2004, 2009; Milliken and others, 2008) have also been constructed without correcting for the effects of subsidence. Holocene shelf sedimentation is another source of error that can be significant (particularly within major incised valleys on the

Table 6. Late Pleistocene and Holocene net shoreline retreat rates for the Texas coast estimated by assuming water depth (fig. 26) approximates shoreline position at past sea-level positions (fig. 25). Effects of subsidence, sedimentation, and erosion are neglected and are significant sources of error. Sea-level ages and elevations are from northern Gulf of Mexico sea level curves published by Balsillie and Donoghue (2004, 2009) and Milliken and others (2008).

| | | Net rate to present (m/yr) | | | | Interval rate from previous position (m/yr) | | | |
|---|---|---|---|---|---|---|---|---|---|
| **Elev. (m msl)** | **Age (ka)** | **Sabine Pass** | **Brazos-Colorado** | **N. Padre Island** | **S. Padre Island** | **Sabine Pass** | **Brazos-Colorado** | **N. Padre Island** | **S. Padre Island** |
| -7 | 7 | -1.0 | -0.2 | -0.1 | -0.1 | -6.3 | -2.0 | -0.7 | -0.8 |
| -10 | 8 | -1.7 | -0.4 | -0.2 | -0.2 | -33.1 | -9.5 | -4.4 | -5.8 |
| -20 | 10 | -7.9 | -2.3 | -1.0 | -1.3 | -55.2 | -40.3 | -26.7 | -18.3 |
| -40 | 11 | -12.2 | -5.7 | -3.4 | -2.9 | -13.6 | -13.2 | -8.2 | -16.2 |
| -60 | 13 | -12.4 | -6.9 | -4.1 | -4.9 | -28.4 | -8.6 | -12.6 | -13.9 |
| -80 | 14 | -13.6 | -7.0 | -4.7 | -5.6 | -4.9 | -3.7 | -5.6 | -2.5 |
| -100 | 16 | -12.5 | -6.6 | -4.8 | -5.2 | - | - | - | - |

inner continental shelf), but is presumed to be minimal in the context of generalized bathymetric contours extending along the entire continental shelf.

This order-of-magnitude approach yields estimated net retreat rates between 16 ka and the present that range from about 5 to 13 m/yr (16 to 41 ft/yr, table 6), reflecting rapid sea-level rise rates and rapid general shoreline retreat during the late Pleistocene and early Holocene. Higher long-term rates are calculated for the upper coast than for the lower coast. Beginning at about 10 ka, net rates generally decrease along the entire coast as the beginning shoreline position date becomes younger; but the trend of higher retreat rates on the upper coast and lower rates on the lower coast is consistent for each period. From 11 ka to present, for example, estimated retreat rates ranged from 3 m/yr (9 ft/yr) along the southern Padre Island transect to 12 m/yr (40 ft/yr) along the Sabine Pass transect. From 8 ka to present, net rates decreased to 0.2 m/yr (0.6 ft/yr) on Padre Island and 1.7 m/yr (5 ft/yr) at Sabine Pass. Published sea-level curves for the northern Gulf of Mexico (Balsillie and Donoghue, 2004, 2009; Milliken and others, 2008) show a reduction in rates of sea-level rise that began between about 8 and 10 ka that coincides with lower estimated rates of postglacial shoreline retreat.

Shoreline change rates can also be estimated for discrete intervals within the general postglacial sea-level rise by comparing past successive sea-level positions and generalized bathymetric contours as a shoreline proxy (table 6). These data show that estimated net retreat rates were very high before 8 ka, ranging from 3 to 55 m/yr (8 to 181 ft/yr) depending on the interval and location (upper coast rates are generally significantly higher than middle- and lower-coast rates). The highest rates of shoreline retreat occurred between 11 ka and 10 ka, when rates ranged between 18 m/yr (60 ft/yr) along the southern Padre Island transect and 55 m/yr (181 ft/yr) along the Sabine Pass transect. Rates between 8 and 7 ka lowered significantly to 0.7 to 6.3 m/yr (2 to 21 ft/yr), as did those since 7 ka (0.1 to 1 m/yr [0.4 to 3.3 ft/yr]). In this context, historical retreat rates averaging 1.7 m/yr (5.6 ft/yr) on the upper Texas coast and 1.0 m/yr (3.2 ft/yr) on the lower Texas coast (calculated from shoreline positions between the 1930s and 2019, table 4) are significantly lower than late Pleistocene to early Holocene retreat estimates during times of rapid postglacial sea-level rise and are similar to retreat rates estimated since the mid-Holocene when sea-level rise rates decreased.

## USING POSTGLACIAL RATES TO PREDICT SHORELINE MOVEMENT

Over postglacial rates of relative sea-level rise that range from 1 to 20 mm/yr at millenial scales (fig. 25), there is a reasonably good empirical relationship ($r^2$ values of 0.48 to 0.78) between rates of relative sea-level rise and net retreat rates for the upper, upper-middle, lower-middle, and lower coast (fig. 27). The best-fit rate of retreat per millimeter per year of sea-level rise increases from south to north along the Texas coast, ranging from 0.8 m/yr (2.8 ft/yr) on the lower coast to 1.8 m/yr (5.9 ft/yr) on the upper coast (fig. 27). These relationships can perhaps be used to predict approximate rates of shoreline retreat that would be expected under various relative sea-level rise scenarios. At historical rates of relative sea-level rise, for example (2 to 4 mm/yr on the lower and lower-middle coast, 3 to 5 mm/yr on the upper-middle coast, and 5 to 7 mm/yr on

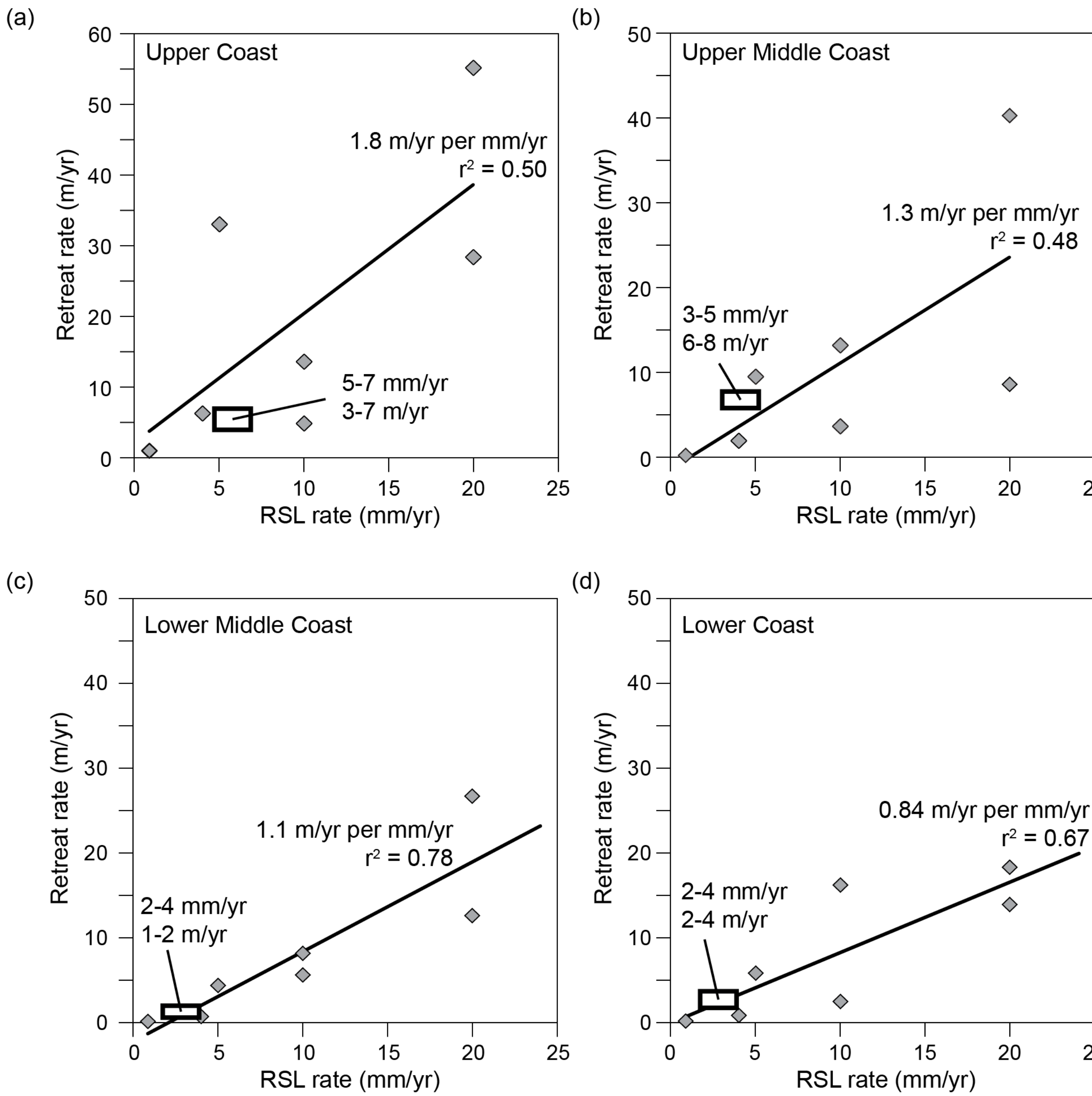


Figure 27. Relationship between postglacial rates of relative sea-level rise (fig. 25) and approximate long-term shoreline retreat rates for (a) the upper-coast, (b) upper-middle coast, (c) lower-middle coast, and (d) lower-coast transects (fig. 27). Boxed areas represent historical retreat rates and historical relative sea-level rise rates.

the upper coast), observed retreat rates of 2 to 4 m/yr (7 to 13 ft/yr) for the lower coast and 1 to 2 m/yr (3 to 7 ft/yr) for the lower-middle coast match predicted rates well (fig. 27c, d). Observed historical retreat rates of 6 to 8 m/yr (20 to 26 ft/yr) for the upper-middle coast are higher than the postglacial relationship would predict, but fall between the postglacial retreat rates calculated for the 8 to 7 ka period (4 mm/yr) and the 10 to 8 ka period (5 mm/yr) (fig. 27b). For the upper coast, historical rates of retreat at 3 to 7 m/yr (10 to 23 ft/yr) are lower than those predicted by the postglacial relationship (fig. 27a), but are nearly identical to the calculated postglacial retreat rate observed for the 8 to 7 ka period when sea-level rose at a similar rate (4 mm/yr).

## CONCLUSIONS

Long-term rates of Texas Gulf shoreline change have been updated through 2019 from a series of shoreline positions that includes those from aerial photography from the 1930s through 2007, ground GPS surveys from the mid-1990s, and airborne lidar surveys conducted in 2000, 2012, and 2019.

Over the 19 storm seasons (2000 to 2018) coinciding with the most recent short-term shoreline monitoring period considered in this report, there were ten tropical storms and six hurricanes that made landfall on the Texas coast, including seven on the upper coast, four on the middle coast, and five on the lower coast. Tropical cyclone frequency was 0.8 per year, which nearly equals the historical frequency. Relative sea-level rise rates at Galveston Pier 21 since 2000, coinciding with the most recent monitoring period, are at the high end of historically observed rates (about 12 mm/yr).

Change rates calculated at 11,722 sites spaced at 50-m intervals averaged net retreat at 1.27 m/yr (4.2 ft/yr) through 2019. Average change rates were more recessional on the upper Texas coast (retreat at 1.71 m/yr [5.6 ft/yr]) than they were on the middle and lower coast (retreat at 0.97 m/yr [3.2 ft/yr]). Annual rates of land loss along the Texas Gulf shoreline average 74 ha/yr (184 ac/yr). Total land loss since 1930, when aerial photography-based shoreline monitoring became possible, is estimated to be 6,627 ha (16,375 ac). For the most recent short-term monitoring period (2000 to 2019), the average net shoreline movement rate is retreat at 1.25 m/yr (4.1 ft/yr), which is similar to the average historical net rate.

Historical shoreline retreat rates calculated from shoreline positions determined from aerial photographs and ground and airborne surveys, when compared to prehistoric rates estimated from bathymetric contour shoreline proxies and past sea-level positions, are significantly lower than late Pleistocene to early-Holocene retreat rates of 2.5 to 55.2 m/yr (8 to 181 ft/yr) but are similar to retreat rates of 0.1 to 1.7 m/yr (0.4 to 5.4 ft/yr) estimated since the mid-Holocene. Postglacial rates of retreat per millimeter per year of relative sea-level rise range from 0.8 m/yr for the lower coast to 1.8 m/yr for the upper coast. This relationship can be used to estimate future rates of Gulf shoreline retreat under various relative sea-level rise scenarios.

## ACKNOWLEDGMENTS

This project was supported by Contract No.16-201-000, Work Order No. B428 from the General Land Office of Texas (GLO) to the Bureau of Economic Geology, The University of Texas at Austin. Jeffrey G. Paine served as the principal investigator. The project was funded through the Coastal Erosion Planning and Response Act (CEPRA) program (Project No. 1662) administered by the GLO. Kelly Brooks (GLO) served as project manager. Bureau researchers John Andrews and Aaron Averett acquired the 2019 airborne lidar survey data. TxDOT pilots Travis Zachary, Carol Foy, Jim Reid, Alan Fenter, and Brian Schoen flew the aircraft. Bureau researchers Tiffany Caudle, John Andrews, and Kutalmis Saylam processed the lidar data and imagery.

## REFERENCES


Anders, F. J., and Byrnes, M. R., 1991, Accuracy of shoreline change rates as determined from maps and aerial photographs: Shore and Beach, v. 59, p. 17–26.

Aronow, S., Fisher, W. L., McGowen, J. H., and Barnes, V. E., 1982, Geologic Atlas of Texas, Houston Sheet: The University of Texas at Austin, Bureau of Economic Geology, scale 1:250,000, 1 sheet.

Balsillie, J. H., and Donoghue, J. F., 2009, Chapter 4: Northern Gulf of Mexico sea-level history for the past 20,000 years: in Holmes, C.W., ed., The Gulf of Mexico, Its Origin, Waters, Biota and Human Impacts: Vol. 1, Geology: Corpus Christi, TX, Harte Research Institute for Gulf of Mexico Studies, p. 53–69.

Balsillie, J. H., and Donoghue, J. F., 2004, High resolution sea-level history for the Gulf of Mexico since the last glacial maximum: Florida Geological Survey, Report of Investigations No. 103, 65 p.

Barnett, T. P., 1983, Global sea level: estimating and explaining apparent changes: in Magoon, O. T., and Converse, H., eds., Coastal Zone ‘83, Proceedings of the Third Symposium on Coastal and Ocean Management, v. 3, p. 2777–2783.

Blake, E. S., and Zelinsky, D. A., 2018, Hurricane Harvey (AL092017): National Hurricane Center Tropical Cyclone Report, 77 p.

Brown, L. F., Jr., Brewton, J. L., and McGowen, J. H., 1975, Geologic Atlas of Texas, Corpus Christi Sheet: The University of Texas at Austin, Bureau of Economic Geology, scale 1:250,000, 1 sheet.

Brown, L. F., Jr., Brewton, J. L., McGowen, J. H., Proctor, C. V., Aronow, S., and Barnes, V.E., 1975, Geologic Atlas of Texas, Beeville-Bay City Sheet: The University of Texas at Austin, Bureau of Economic Geology, scale 1:250,000, 1 sheet.

Brown, L. F., Jr., Brewton, J. L., White, W. A., and Owens, F., 1976, Geologic Atlas of Texas, McAllen-Brownsville Sheet: The University of Texas at Austin, Bureau of Economic Geology, scale 1:250,000, 1 sheet.

Bruun, P., 1954, Coastal erosion and development of beach profiles: Technical Memorandum, v. 44, Beach Erosion Board, U. S. Army Corps of Engineers, 82 p.

Bruun, P., 1962, Sea-level rise as a cause of shore erosion: Proceedings, American Society of Civil Engineers, Journal of the Waterways and Harbors Division, v. 88, p. 117–130.

Bruun, P., 1988, The Bruun rule of erosion by sea-level rise: a discussion of large-scale two- and three-dimensional usages: Journal of Coastal Research, v. 4, p. 627–648.

Caudle, T., and Paine, J. G., 2012, Pre-college student involvement in Texas coastal research: Gulf Coast Association of Geological Societies Transactions, v. 62, p. 27–38.

Caudle, T., and Paine, J. G., 2017, Applications of coastal data collected in the Texas High School Coastal Monitoring Program (THSCMP): Journal of Coastal Research, v. 33, no. 3, p. 738–746. DOI: 10.2112/JCOASTRES-D-16-00033.1.

Cazenave, A., and Nerem, R. S., 2004, Present-day sea level change: observations and causes: Reviews of Geophysics, v. 42, RG3001. doi: 1029/2003RG000139, 20 p.

Cazenave, A., Dieng, H.-B., Meyssignac, B., von Schuckmann, K., Decharme, B., and Berthier, E., 2014, The rate of sea-level rise: Nature Climate Change, v. 4, p. 358-361.

Church, J. A., Clark, P. U., Cazenave, A., Gregory, J. M., Jevrejeva, S., Levermann, A., Merrifield, M. A., Milne, G. A., Nerem, R. S., Nunn, P. D., Payne, A. J., Pfeffer, W. T., Stammer, D., and Unnikrishnan, A. S., 2013, Sea Level Change: in Stocker, T. F., Qin, D., Plattner, G.-K., Tignor, M., Allen, S. K., Boschung, J., Nauels, A., Xia, Y., Bex, V., and Midgley, P.M., eds., Climate Change 2013: The Physical Science Basis: Contribution of Working Group I to the Fifth Assessment Report of the Intergovernmental Panel on Climate Change. Cambridge, United Kingdom and New York, NY, USA: Cambridge University Press, 1137–1216.

Church, J. A., and White, N. J., 2006, A 20$^{th}$ century acceleration in global sea-level rise: Geophysical Research Letters, v. 33: L01602. doi: 10.1029/2005GL024826.

Church, J. A., and White, N. J., 2011, Sea-level rise from the late 19th to the early 21st century: Surveys in Geophysics, v. 32, p. 585-602. doi: 10.1007/s10712-011-9119-1.

Cooper, J. A. G., and Pilkey, O. H., 2004, Sea-level rise and shoreline retreat: time to abandon the Bruun Rule: Global and Planetary Change, v. 43, p. 157–171.

Crowell, M., Leatherman, S. P., and Buckley, M. K., 1991, Historical shoreline change: error analysis and mapping accuracy: Journal of Coastal Research, v. 7, no. 3, p. 839–852.

Emery, K. O., 1980, Relative sea levels from tide-gauge records: Proceedings, National Academy of Sciences, USA, v. 77: p. 6968–6972.

FitzGerald, D. M., Fenster, M. S., Argow, B. A., and Buynevich, I. V., 2008, Coastal impacts due to sea-level rise: Annual Review of Earth and Planetary Sciences, v. 36, p. 601–647.

Gibeaut, J. C., and Caudle, T., 2009, Defining and mapping foredunes, the line of vegetation, and shorelines along the Texas Gulf Coast: Texas A&M University Corpus Christi, Harte Research Institute and The University of Texas at Austin, Bureau of Economic Geology, final report prepared for the Texas General Land Office contract no. 07-005-22 and National Oceanic and Atmospheric Administration award no. NA06NOS4190219, 14 p.

Gibeaut, J. C., Gutierrez, R., and Hepner, T., 2002, Threshold conditions for episodic beach erosion along the southeast Texas coast: Gulf Coast Association of Geological Societies Transactions, v. 52, p. 323–335.

Gibeaut, J. C., Hepner, T., Waldinger, R., Andrews, J., Gutierrez, R., Tremblay, T. A., and Smyth, R., 2001, Changes in Gulf shoreline position, Mustang and North Padre Islands, Texas: The University of Texas at Austin, Bureau of Economic Geology, Report to the Texas Coastal Coordination Council and the General Land Office, contract no. 00-002r, 29 p.

Gibeaut, J. C., White, W. A., Hepner, T., Gutierrez, R., Tremblay, T. A., Smyth, R. A., and Andrews, J., 2000, Texas Shoreline Change Project: Gulf of Mexico shoreline change from the Brazos River to Pass Cavallo: The University of Texas at Austin, Bureau of Economic

Geology, Report to the Texas Coastal Coordination Council and the General Land Office, contract no. NA870Z0251, 32 p.

Gornitz, V., Lebedeff, S., and Hansen, J., 1982, Global sea level trend in the past century: Science, v. 215, p. 1611–1614.

Gornitz, V., and Lebedeff, S., 1987, Global sea-level changes during the past century: in Nummedal, D., Pilkey, O. H., and Howard, J. D., eds., Sea level fluctuation and coastal evolution: Society of Economic Paleontologists and Mineralogists Special Publication 41, p. 3–16.

Gutenberg, B., 1941, Changes in sea level, postglacial uplift, and mobility of the Earth's interior: Geological Society of America Bulletin, v. 52, p. 721–772.

Hayes, M. O., 1967, Hurricanes as geological agents: case studies of hurricanes Carla, 1961, and Cindy, 1963: The University of Texas at Austin, Bureau of Economic Geology, Report of Investigations No. 61, 54 p.

Himmelstoss, E. A., Farris, A. S., Henderson, R. E., Kratzmann, M. G., Ergul, Ayhan, Zhang, Ouya, Zichichi, J. L., Thieler, E. R., 2018, Digital Shoreline Analysis System (version 5.0): U.S. Geological Survey software release, https://code.usgs.gov/cch/dsas.

Holcombe, T. L., and Arias, C., 2009, Bathymetry of Texas-Louisiana continental shelf and coastal regions compatible with geographic information systems – bathymetry (version 2): Texas A&M University, Department of Oceanography.

LeBlanc, R. J. and Hodgson, W. D., 1959, Origin and development of the Texas shoreline: Gulf Coast Association of Geological Societies Transactions, v. 9, p. 197–220.

Leuliette, E. W., and Miller, L., 2009, Closing the sea level rise budget with altimetry, Argo, and GRACE: Geophysical Research Letters, v. 36, L04608. doi:10.1029/2008GL036010.

Leuliette, E. W. and Willis, J. K., 2011, Balancing the sea level budget: Oceanography, v. 24, no. 2, p. 122–129. doi:10.5670/oceanog.2011.32.

Lyles, S. D., Hickman, L. E., Jr., and Debaugh, H. A., Jr., 1988, Sea level variations for the United States, 1855-1986: National Ocean Service, Rockville, Maryland, 182 p.

Milliken, K. T., Anderson, J. B., and Rodriguez, A. B., 2008, A new composite Holocene sea-level curve for the northern Gulf of Mexico: in Anderson, J.B., and Rodriguez, A. B., eds., Response of Upper Gulf Coast Estuaries to Holocene Climate Change and Sea-Level Rise: Geological Society of America Special Paper 443, p. 1–11. doi: 10.1130/2008.2443(01).

Moore, L. J., 2000, Shoreline mapping techniques: Journal of Coastal Research, v. 16, no. 1, p. 111–124.

Morton, R. A., 1974, Shoreline changes on Galveston Island (Bolivar Roads to San Luis Pass), an analysis of historical changes of the Texas Gulf shoreline: The University of Texas at Austin, Bureau of Economic Geology, Geological Circular 74-2, 34 p.

Morton, R. A., 1975, Shoreline changes between Sabine Pass and Bolivar Roads: The University of Texas at Austin, Bureau of Economic Geology, Geological Circular 75-6, 43 p.

Morton, R. A., 1977, Historical shoreline changes and their causes, Texas Gulf Coast: Gulf Coast Association of Geological Societies Transactions, v. 27, p. 352–364. Reprinted as Bureau of Economic Geology Geological Circular 77-6, 13 p.

Morton, R. A., 1997, Gulf shoreline movement between Sabine Pass and the Brazos River, Texas: 1974 to 1996: The University of Texas at Austin, Bureau of Economic Geology, Geological Circular 97-3, 46 p.

Morton, R. A., Leach, M. P., and Cardoza, M. A., 1993, Monitoring beach changes using GPS surveying techniques: Journal of Coastal Research, v. 9, p. 702-720.

Morton, R. A., Miller, T. L., and Moore, L. J., 2004, National assessment of shoreline change, part 1: historical shoreline changes and associated coastal land loss along the U.S. Gulf of Mexico: U.S. Geological Survey Open-File Report 2004-1043, 42 p.

Morton, R. A., and Paine, J. G., 1985, Beach and vegetation-line changes at Galveston Island, Texas: erosion, deposition, and recovery from Hurricane Alicia: The University of Texas at Austin, Bureau of Economic Geology Geological Circular 85-5, 39 p.

Morton, R. A., and Paine, J. G., 1990, Coastal land loss in Texas: an overview: Transactions, Gulf Coast Association of Geological Societies, v. 40, p. 625-634.

Morton, R. A., Paine, J. G., and Gibeaut, J. C., 1994, Stages and durations of post-storm beach recovery, southeastern Texas coast, U.S.A.: Journal of Coastal Research, v. 10, p. 884–908.

Morton, R. A., and Pieper, M. J., 1975a, Shoreline changes on Brazos Island and South Padre Island (Mansfield Channel to mouth of the Rio Grande), an analysis of historical changes of the Texas Gulf shoreline: The University of Texas at Austin, Bureau of Economic Geology, Geological Circular 75-2, 39 p.

Morton, R. A., and Pieper, M. J., 1975b, Shoreline changes in the vicinity of the Brazos River delta (San Luis Pass to Brown Cedar Cut): The University of Texas at Austin, Bureau of Economic Geology, Geological Circular 75-4, 47 p.

Morton, R. A., and Pieper, M. J., 1976, Shoreline changes on Matagorda Island and San Jose Island (Pass Cavallo to Aransas Pass): The University of Texas at Austin, Bureau of Economic Geology, Geological Circular 76-4, 42 p.

Morton, R. A., and Pieper, M. J., 1977a, Shoreline changes on Mustang Island and North Padre Island (Aransas Pass to Yarborough Pass): The University of Texas at Austin, Bureau of Economic Geology, Geological Circular 77-1, 45 p.

Morton, R. A., and Pieper, M. J., 1977b, Shoreline changes on central Padre Island (Yarborough Pass to Mansfield Channel): The University of Texas at Austin, Bureau of Economic Geology, Geological Circular 77-2, 35 p.

Morton, R. A., Pieper, M. J., and McGowen, J. H., 1976, Shoreline changes on Matagorda Peninsula (Brown Cedar Cut to Pass Cavallo): The University of Texas at Austin, Bureau of Economic Geology, Geological Circular 76-6, 37 p.

Nerem, R. S., Beckley, B. D., Fasullo, J. T., Hamlington, B. D., Masters, D., and Mitchum, G. T., 2018, Climate-change-driven accelerated sea-level rise detected in the altimeter era:

Proceedings of the National Academy of Sciences of the United States of America, v. 115, no. 9, p. 2022-2025. doi: 10.1073/pnas.1717312115.

Paine, J. G., 1991, Late Quaternary depositional units, sea level, and vertical movement along the central Texas coast: Ph. D. dissertation, University of Texas at Austin, Austin, Texas, 256 p.

Paine, J. G., 1993, Subsidence of the Texas coast: inferences from historical and late Pleistocene sea levels: Tectonophysics, v. 222, p. 445–458.

Paine, J. G., Caudle, T., and Andrews, J., 2013, Shoreline, beach, and dune morphodynamics, Texas Gulf coast: The University of Texas at Austin, Bureau of Economic Geology, Final Report prepared for General Land Office under contract no. 09-242-000-3789, 64 p.

Paine, J. G., Caudle, T., and Andrews, J., 2014, Shoreline movement along the Texas Gulf coast, 1930's to 2012: The University of Texas at Austin, Bureau of Economic Geology, Final Report prepared for General Land Office under contract no. 09-074-000, 52 p. + CD-ROM.

Paine, J. G., Caudle, T., and Andrews, J. R., 2016, Shoreline movement in the Copano, San Antonio, and Matagorda Bay systems, central Texas coast, 1930s to 2010s: The University of Texas at Austin, Bureau of Economic Geology, Final Report prepared for General Land Office under contract no. 13-258-000-7485, 72 p.

Paine, J. G., Caudle, T., and Andrews, J. R., 2017, Shoreline and sand storage dynamics from annual airborne lidar surveys, Texas Gulf Coast: Journal of Coastal Research, v. 33, no. 3, p. 487–506. DOI: #10.2112/JCOASTRES-D-15-00241.1.

Paine, J. G., Mathew, S., and Caudle, T., 2011, Texas Gulf shoreline change rates through 2007: The University of Texas at Austin, Bureau of Economic Geology, Report prepared under General Land Office contract no. 10-041-000-3737 and National Oceanic and Atmospheric Administration award no. NA09NOS4190165, 38 p. + CD-ROM.

Paine, J. G., Mathew, S., and Caudle, T., 2012, Historical shoreline change through 2007, Texas Gulf coast: rates, contributing causes, and Holocene context: GCAGS Journal, v. 1, p. 13-26.

Paine, J. G., and Morton, R. A., 1989, Shoreline and vegetation-line movement, Texas Gulf Coast, 1974 to 1982: The University of Texas at Austin, Bureau of Economic Geology Geological Circular 89-1, 50 p.

Peltier, W. R., and Tushingham, A. M., 1989, Global sea level rise and the greenhouse effect: might they be connected?: Science, v. 44, p. 806-810.

Penland, S., and Ramsey, K., 1990, Sea-level rise in Louisiana and the Gulf of Mexico: 1908-1988: Journal of Coastal Research, v. 6, no. 2, p. 323–342.

Price, W. A., 1956, Hurricanes affecting the coast of Texas from Galveston to the Rio Grande: U.S. Army Corps of Engineers, Beach Erosion Board, Technical Memorandum No. 78, 35 p.

Roth, D., 2010, Texas hurricane history: National Weather Service, Camp Springs, Maryland, 83 p. http://origin.hpc.ncep.noaa.gov/research/txhur.pdf

Shalowitz, A. L., 1964, Shore and beach boundaries: U.S. Department of Commerce, Publication 10-1, 749 p.

Shepard, F. P., 1960, Rise of sea level along northwest Gulf of Mexico: in Shepard, F. P., Phleger, F. B., and van Andel, T.H., eds., Recent Sediments, Northwest Gulf of Mexico: Tulsa, Oklahoma, American Association of Petroleum Geologists, pp. 338–344.

Simpson, R. H., and Riehl, H., 1981, The hurricane and its impact: Baton Rouge, Louisiana State University Press, 398 p.

Snay, R., Cline, M., Dillinger, W., Foote, R., Hilla, S., Kass, W., Ray, J., Rohde, J., Sella, G., and Soler, T., 2007, Using global positioning system-derived crustal velocities to estimate rates of absolute sea level change from North American tide gauge records: Journal of Geophysical Research, v. 112, B04409, 11 p. doi: 10.1029/2006JB004606.

Swanson, R. L., and Thurlow, C. I, 1973, Recent subsidence rates along the Texas and Louisiana coast as determined from tide measurements: Journal of Geophysical Research, v. 78, p. 2665–2671.

U.S. Army Corps of Engineers, 2017, 2016 USACE NCMP topobathy lidar DEM: Gulf Coast (TX), Joint Airborne Lidar Bathymetry Technical Center of Expertise (JALBTCX), Charleston, SC.

## APPENDIX: 2019 AIRBORNE LIDAR AND IMAGERY SURVEY

Researchers from the Bureau of Economic Geology (Bureau) acquired high-resolution airborne lidar data of the Texas Gulf coast on 11 days between April 2, 2019 and June 2, 2019. Data were collected using the Bureau's airborne lidar and imagery system (Chiroptera, fig. A1), which can collect topographic lidar data, shallow bathymetric lidar data, and high-resolution imagery simultaneously. The topographic lidar scanner operates at a wavelength of 1 µm, a pulse rate as high as 400 kHz, and an incident angle (from vertical) of 28 to 40 degrees. It can operate to a maximum height of about 1,500 m (5,000 ft), allowing the system to be used to rapidly scan large areas with a range accuracy of about 2 cm over a flat target. The bathymetric lidar scanner operates at a shorter wavelength (0.515 µm) and a lower pulse rate (35 kHz). The shorter wavelength allows the laser to penetrate water of reasonable clarity. After the laser reflects off the bottom surface and back to the source, the transit-time difference between water-surface and water bottom reflections can be used to determine water depths to a flat-bottom accuracy of about 15 cm (6 in). Also mounted in the Chiroptera chassis is a Hasselblad DigiCAM 50 megapixel natural color (RGB) camera that acquires frame images at a resolution of 8,176 by 6,132 pixels.


Figure A1. The Bureau's Chiroptera airborne lidar and imagery system. The system was built for the Bureau by Airborne Hydrography AB and delivered in July 2012.

Acquisition of topographic lidar data over a swath along the Texas Gulf of Mexico beach and dune system, bathymetric lidar data over a swath along the Gulf of Mexico shoreline and two nearshore areas, and topographic and bathymetric lidar data at five beaches in Corpus Christi, Aransas, and Matagorda Bays (fig. 4) were the principal objectives of this project. Aerial imagery was acquired for reference and interpretational purposes.

We acquired two higher-altitude topographic laser swaths along the 590 km (367 mi) of Texas Gulf shoreline from the beach landward across the dunes, and two lower-altitude bathymetric laser swaths from the beach seaward a few hundred meters into shallow water. The bathymetric survey areas extended farther seaward along GLO's two 10-km-long segments of special interest at southern Padre Island (to about 1,500 m [5,000 ft] offshore) and at Surfside (to about 3,500 m [11,500 ft] offshore). Two lower-altitude passes were conducted at five bay beaches: University Beach, North Beach, and McGee Beach in Corpus Christi Bay; Rockport Beach in Aransas Bay; and Indianola Beach in Matagorda Bay (fig. 4).

Airborne lidar data and supplemental RGB imagery were acquired during several deployments between April 2 and June 2, 2019 (table A1) using a single-engine Cessna Stationaire 206 aircraft (tail number N147TX) owned and operated by the Texas Department of Transportation (TxDOT). The aircraft was flown from the following coastal Texas airports: Corpus Christi, Rockport, Bay City, Angleton, Galveston, Harlingen, Laguna Vista, and Port Arthur. Middle Texas coast survey areas (mouth of the Colorado River to the northern boundary of Padre Island National Seashore) were flown on April 2-4 and April 8 (MTC, table A1). Upper Texas coast survey areas (Sabine Pass to the mouth of the Colorado River) were flown on April 8-9, May 16, and June 2 (UTC, table A1). South Texas coastal areas (northern boundary of Padre Island National Seashore to the Rio Grande) were flown on April 16, 18, and 19 (STC, table A1).

Extended bathymetric surveys were conducted at Surfside beach on April 11, 2019 (fig. 4 and table A1) and southern Padre Island April 19, 2019 (fig. 4 and table A1). Rockport Beach was

Table A1. Flight dates, survey areas flown, and GPS base stations used for the 2019 airborne lidar survey of the Texas coast.

| Date | Flight # | Airport | Location | GPS Base Stations |
|---|---|---|---|---|
| 4/2/2019 | 1 | Corpus/Rockport | MTC | txcc, txpo, txpv, txrt |
| | 2 | Corpus/Rockport | MTC | txcc, txpo, txpv, txrt |
| 4/3/2019 | 1 | Corpus | MTC | txcc, txpo, txrt |
| 4/4/2019 | 1 | Corpus/Rockport | MTC/bay beach | txcc, txpo, txpv, txrt |
| | 2 | Rockport/Austin | MTC | txcc, txpo, txpv, txrt |
| 4/8/2019 | 1 | Bay City | MTC | txbc, txpv, mata |
| | 2 | Bay City | MTC/bay beach/ UTC | txbc, txpv, mata |
| | 3 | Bay City | UTC | txag, txbc, mata |
| 4/9/2019 | 1 | Bay City/Angelton | UTC | txag, txbc, mata |
| | 2 | Angelton/Galveston | UTC | txag, txlm, txga |
| 4/11/2019 | 1 | Galveston/Angelton | Surfside offshore | txag, txlm, txga |
| | 2 | Angelton/Galveston | Surfside offshore | txag, txlm, txga |
| 4/16/2019 | 1 | Harlingen | STC | ptmn, txrv, txln, txbv |
| 4/18/2019 | 1 | Harlingen/Laguna Vista | STC | ptmn, txrv, txln, txbv |
| | 2 | Laguna Vista/Harlingen | STC | ptmn, txrv, txln, txbv |
| 4/19/2019 | 1 | Harlingen | STC | ptmn, txrv, txln, txbv |
| | 2 | Harlingen | SPI offshore | ptmn, txrv, txln, txbv |
| 5/16/2019 | 1 | Austin/Port Arthur | UTC | txlm, txga, txac, txpt |
| | 2 | Port Arthur/Galveston | UTC | txlm, txga, txac, txpt |
| 6/2/2019 | 1 | Austin/Galveston | bay beach/UTC | txcc, txpo, txag, txlm, txga |
| | 2 | Galveston/Austin | UTC | txag, txlm, txga |
| | | | | |

surveyed during the April 4th flight, Indianola Beach on April 8th, and the Corpus Christi Bay beaches (University, North, and McGee) on June 2, 2019 (table A1).

Flight elevations averaging 750 m (2,460 ft) above ground level and a topographic laser pulse rate of 150 kHz were used for topographic lidar data collection along the 590 km (367 mi) of Texas Gulf shoreline. Bathymetric lidar data collection flights along the Gulf of Mexico nearshore, southern Padre Island and Surfside special interest areas, and bay beaches were flown at 400 m (1,300 ft) above ground level using a topographic laser pulse rate of 250 kHz and a bathymetric laser pulse rate of 35 kHz.

Thirteen Continuously Operating Reference Stations (CORS) were used during the lidar surveys (fig. 4) for differential corrections. TxDOT set the following stations to record data at a 1-second interval during the survey: Anahuac (txac), Angleton (txag), Bay City (txbc), Brownsville (txbv), Corpus Christi (txcc), Galveston (txga), La Marque (txlm), Laguna Vista (txln), Port Aransas (txpo), Port Arthur (txpt), Port Lavaca (txpv), Rockport (txrt), and Raymondville (txrv). These stations typically record data at a 15- or 30-second intervals. GPS base stations (Trimble Net R9 receivers and antennas) recording at a 1-second interval were deployed at Matagorda Bay Nature Park (mata) and Port Mansfield (ptmn) for additional GPS ground control in areas too distant from CORS receivers. At least three base stations were used to process data during each flight (Table A1).